A Model for QCD at High Density and Large Quark Mass

Roberto De Pietri,[1,2] Alessandra Feo,[1,2] Erhard Seiler,[3] and Ion-Olimpiu Stamatescu[4,5]

[1]*Dipartimento di Fisica, Università di Parma, Italy*
[2]*INFN Gruppo Collegato di Parma, Italy*
[3] *Max-Planck-Institut für Physik (Werner Heisenberg Institut), München, Germany*
[4]*FEST - Protestant Institute for Interdisciplinary Research, Heidelberg, Germany*
[5]*Institut für Theoretische Physik der Universität, Heidelberg, Germany*

(Dated: February 1, 2022)

We study the high density region of QCD within an effective model obtained in the frame of the hopping parameter expansion and choosing Polyakov type of loops as the main dynamical variables representing the fermionic matter. To get a first idea of the phase structure, the model is analyzed in strong coupling expansion and using a mean field approximation. In numerical simulations, the model still shows the so-called sign problem, a difficulty peculiar to non-zero chemical potential, but it permits the development of algorithms which ensure a good overlap of the Monte Carlo ensemble with the true one. We review the main features of the model and present calculations concerning the dependence of various observables on the chemical potential and on the temperature, in particular of the charge density and the diquark susceptibility, which may be used to characterize the various phases expected at high baryonic density. We obtain in this way information about the phase structure of the model and the corresponding phase transitions and cross over regions, which can be considered as hints for the behaviour of non-zero density QCD.

PACS numbers: 11.15.Ha, 12.38.Gc, 12.38.Aw

arXiv:0705.3420v2 [hep-lat] 9 Sep 2007

I. INTRODUCTION

The exploration of the phase diagram of matter at non-zero baryon density is a challenging and interesting problem. In particular, it has been emphasized that quark matter at extremely high density may behave as a color superconductor (see Ref.[1] for a recent review on the subject and references therein). Moreover, it is also expected that the phase diagram in the temperature-density plane shows multiple phases separated by various critical lines and, except for the high T, small μ region, not much is known about their exact position and nature.

Lattice gauge theory calculations in various implementations that try to evade the sign problem generated by the non-zero chemical potential have been mostly performed at small baryon density and high temperature, where they agree reasonably well with each other. Here there is good evidence for the presence of a crossover instead of a sharp deconfining transition. At large μ (baryon density), however, there are only few numerical results which need to be corroborated by using different methods. See [2] for a review.

The aim of this work is to understand the phase structure of high density, strongly interacting matter. Most work on QCD at non-zero density proceeds from the $\mu = 0$, $T \sim T_c$ region and attempts to go as far as possible in the $\mu > 0$ domain. As an alternative one may consider the possibility to start from the large μ domain and try to reach the region of interest from above. In the spirit of the $\mu = 0$ quenched approximation a 'non-zero density quenched approximation' for $\mu > 0$ based on the double limit $M \to \infty$, $\mu \to \infty$, $\zeta \equiv \exp(\mu - \ln M)$: fixed [3, 4] has been considered. This implements a static, charged background, which influences the gluonic dynamics [4, 5]. The present model [6] represents a systematic extension of the above considerations: the gluonic vacuum is enriched by the effects of dynamical quarks of large (but not infinite) mass, providing a large net baryonic charge. In [7] and in the present paper we explore the phase structure of the model, as a first step in understanding the properties of such a background.

This model can be derived as a $1/M$ expansion of QCD at large μ around the unphysical limit of infinitely heavy quarks. However, it is more realistic to understand it as an approximation whose justification relies on the predominant role of the gluonic dynamics. We want to understand how this dynamics is influenced by the presence of charged matter. This would allow, among other things, to study the effect of dense, heavier background baryonic charges on light quarks and hadrons.

The main ingredient of the model are Polyakov-type loops, capturing the effect of heavy quarks with low mobility. The model still has a sign problem, but being based on the variables which are especially sensitive to the physics of dense baryonic matter it allows for reweighting algorithms which ensure a good overlap of the Monte Carlo ensemble with the true one.

The paper is organized as follows. In Sec.II we study the high density region of QCD within an effective model obtained by an expansion in the hopping parameter κ of the fermionic determinant up to next-to leading order, κ^2. In Sec.III the model is analyzed using first a strong coupling expansion and then a mean field approximation just to get a first idea of the phase diagram and to compare with numerical simulations.

Sec.IV shows results of the numerical simulations. Here the model shows the so-called sign problem but due to the factorization of the fermionic determinant it permits to develop very efficient local algorithms and achieve large statistics. The dependence of various observables on the chemical potential and the temperature is studied and we show a tentative phase diagram at large mass and high baryon density. Conclusions and outlook are given in Sec. V.

II. QCD AT LARGE CHEMICAL POTENTIAL

.

A. QCD at non-zero μ

In this study we use the grand canonical formulation of QCD, i.e., we introduce the chemical potential μ as a (bare) parameter. The QCD grand canonical partition function with Wilson fermions at $\mu > 0$ is:

$$\mathcal{Z}(\beta,\kappa,\gamma_G,\gamma_F,\mu) = \int [DU]\, \mathrm{e}^{-S_G(\beta,\gamma_G,\{U\})}\, \mathcal{Z}_F(\kappa,\gamma_F,\mu,\{U\})\,, \quad (2.1)$$

$$S_G(\beta,\gamma_G,\{U\}) = -\frac{\beta}{N_c}\, Re\, \mathrm{Tr}\, \left(\frac{1}{\gamma_G}\sum_{j>i=1}^{3} P_{ij} + \gamma_G \sum_i P_{i4}\right)\,, \quad (2.2)$$

$$\mathcal{Z}_F(\kappa,\gamma_F,\mu,\{U\}) = \mathrm{Det}\, W(\kappa,\gamma_F,\mu,\{U\})\,, \quad (2.3)$$

$$W_{ff'} = \delta_{ff'}[1 - \kappa_f \sum_{i=1}^{3} (\Gamma_{+i}\, U_i\, T_i + \Gamma_{-i}\, T_i^*\, U_i^*) - \kappa_f\, \gamma_F\, \left(\mathrm{e}^{\mu_f}\, \Gamma_{+4}\, U_4\, T_4 + \mathrm{e}^{-\mu_f}\, \Gamma_{-4}\, T_4^*\, U_4^*\right)]\,,$$

$$\Gamma_{\pm\mu} = 1 \pm \gamma_\mu,\ \ \gamma_\mu = \gamma_\mu^*,\ \gamma_\mu^2 = 1\,,$$

$$\kappa = \frac{1}{2(M + 3 + \gamma_F\, \cosh\mu)} = \frac{1}{2(M_0 + 3 + \gamma_F)}\,,$$

where we have specialized S_G for Wilson's plaquette (P) action and used a certain definition of the Wilson term in W. Here M is the 'bare mass', M_0 the bare mass at $\mu = 0$, f is the flavor index, U_μ denote the link variables and T_μ lattice translations. For the sake of generality and the discussion in section III.B we also introduced coupling anisotropies γ_G, γ_F which however will be set to 1 elsewhere. All quantities are understood in units of the (spatial) lattice spacing a unless explicitly specified otherwise. The exponential prescription for μ ensures canceling of divergences in the small a limit [8]. A non-zero physical temperature T is introduced as

$$a\, T = \frac{\gamma_{phys}}{N_\tau}\,, \quad (2.4)$$

where γ_{phys} is the physical cutoff anisotropy defined by an appropriate renormalization of the coupling anisotropies [9], and N_τ the 'length' of the (periodic) temporal lattice size.

The fermionic coupling matrix W fulfills:

$$\gamma_5 W(\mu)\gamma_5 = W(-\mu)^*,\ \ \mathrm{Det}\, W(\mu) = \mathrm{Det}\, W(-\mu)^* \quad (2.5)$$

where the $*$ conjugation above is understood in the lattice and color indices, that is $U^*_{n,\nu} = U^\dagger_{(n+\nu),-\nu}$. At $\mu \neq 0$ the determinant is complex (while, due to the symmetries of the Yang-Mills integration the full partition function remains real).

Numerical simulations are based on defining an efficient importance sampling of the configurations. Since the integrand (for simplicity we shall still call it 'Boltzmann factor'):

$$B = \mathrm{e}^{-S_G(\beta,\{U\})}\, \mathcal{Z}_F(\kappa,\mu,\{U\}) \quad (2.6)$$

is not a real, positive definite number it does not define a probability measure for the Yang-Mills integration. There have been a number of methods devised to cope with this problem, which all involve simulating a different ensemble and correcting the results either by continuing in μ or by redefining the observables.

Continuation methods use the Taylor expansion [10], [11] or more sophisticate expansions [12] to enter the region of real, non-zero μ by fitting the coefficients from $\mu = 0$ simulations [10] or from simulations at imaginary μ [11] [12]. They rely on correctly identifying the analytic properties of the partition function and the various expectation values. Due to the noise in determining the expansion coefficients the quality of the continuation degrades rapidly with increasing (real) μ. Since the simulations are done with dynamical quarks the statistics is limited.

The so called 'reweighting method' proceeds by choosing a positive definite measure B_0 obtained by splitting the original 'Boltzmann factor' according to

$$B = B_0 w_0\,. \quad (2.7)$$

B_0 is used to produce an ensemble of configurations $C_n^0 = \{U\}_n^0$ (where n indexes the configurations) to be reweighted by the complex numbers $w_{0,n} = B_n/B_{0,n}$ associated with the configurations C_n^0 in calculating expectation values:

$$\langle O\rangle = \frac{\langle w_0 O\rangle_0}{\langle w_0\rangle_0}\,, \quad (2.8)$$

with O some observable and $\langle\dots\rangle_0$ denoting averages over the ensemble C^0. Notice that w_0 is both complex and non-local since it comes from the fermionic determinant. The $\langle\dots\rangle_0$ averages contain therefore alternating contributions with large cancellations (the 'sign problem'). Moreover, the reweighting can correct an underestimated contribution in the C^0 ensemble, but fails if the underestimation is too drastic (the 'overlap problem'). In both cases the problems are aggravated by the non-locality of w_0 which makes it difficult to achieve high statistics.

Calculations based on various implementations of the reweighting method [13] have been performed mainly at small μ, where they agree reasonably well with other methods (analytic expansion [11], [12], [14]). At large μ, however, there are only few numerical results yet, mainly based on only one method [15] and corroboration by different methods is missing.

At large μ the behaviour of QCD quantities may however be dominated by certain factors in the fermionic determinant which lead to a simpler model that is actually easier to simulate. In its lowest order this model is considered to define what can be called 'quenched, non-zero density QCD' [4]. The model is based on an analytic expansion of QCD (the

hopping parameter expansion) and involves the Polyakov loop variables of the theory, which in many setups are thought to catch important effects of the fermionic matter [16]. This, and its suitability for numerical simulations makes this model interesting for study. Moreover it may give us hints for improving the algorithms for the full QCD at non-zero density.

In the next subsections we shall recall the hopping parameter expansion and describe the model.

B. Hopping parameter expansion of the fermionic determinant

The large mass (hopping parameter) expansion of QCD arises from an expansion of the logarithm of the fermionic determinant exhibiting only closed loops:

$$\begin{aligned} \mathrm{Det}\, W &= \exp(\mathrm{Tr}\, \ln W) \qquad (2.9)\\ &= \exp\left[-\sum_{l=1}^{\infty}\sum_{\{\mathcal{C}_l\}}\sum_{s=1}^{\infty}\frac{\left(\kappa_f^l g^f_{\mathcal{C}_l}\right)^s}{s}\,\mathrm{Tr}_{\,\mathrm{D,C}}\mathcal{L}^s_{\mathcal{C}_l}\right]\\ &= \prod_{l=1}^{\infty}\prod_{\{\mathcal{C}_l\}}\prod_f \mathrm{Det}_{\,\mathrm{D,C}}\left(\mathbf{1} - (\kappa_f)^l g^f_{\mathcal{C}_l}\mathcal{L}_{\mathcal{C}_l}\right). \end{aligned}$$

Here $\mathcal{C}_l$ are distinguishable, non-exactly-self-repeating closed paths of length l and s is the number of times a loop $\mathcal{L}_{\mathcal{C}_l}$ covers $\mathcal{C}_l$. With λ denoting the links along $\mathcal{C}_l$ we have

$$\mathcal{L}_{\mathcal{C}_l} = \left(\prod_{\lambda\in\mathcal{C}_l}\Gamma_\lambda U_\lambda\right)^s, \qquad (2.10)$$

$$\begin{aligned} g^f_{\mathcal{C}_l} &= \left(\epsilon\, \mathrm{e}^{\pm N_\tau \mu_f}\right)^r \text{ if } \mathcal{C}_l = \text{'Polyakov r-path'},\\ &= 1 \text{ otherwise}. \qquad (2.11) \end{aligned}$$

The index D, C in (2.9) means that the traces (the determinants) are understood both over Dirac and color indices. A 'Polyakov r-path' closes over the lattice in the ± 4 direction with winding number r and periodic(antiperiodic) b.c. ($\epsilon = +1(-1)$). We assume periodic b.c. in the 'spatial' directions. Notice that, since the determinant is a polynomial in κ this expansion terminates at the order $dN_LN_cn_f$ with $d = 2, 4$ the dimension, N_L the lattice volume, N_c the number of colors and n_f the number of flavors. For details see [17].

C. The massive, dense limit of the fermionic determinant

The double limit [3]

$$\kappa \to 0,\ \mu \to \infty,\ \ \kappa\, \mathrm{e}^{\,\mu} \equiv \zeta :\ \text{fixed} \qquad (2.12)$$

produces a static, dense, charged background on the lattice, and has been therefore proposed and studied as a non-zero density quenched approximation [4, 5]. Note that the pure Yang-Mills limit corresponds to $\zeta = 0$, which for fixed nonzero κ requires $\mu \to -\infty$.

In the limit (2.12) the fermionic determinant simplifies considerably, e.g., for 1 flavor we have:

$$\begin{aligned} \mathcal{Z}_F^{[0]}(C,\{U\}) &= \exp\left[-2\sum_{\{\vec{x}\}}\sum_{s=1}^{\infty}\frac{(\epsilon C)^s}{s}\,\mathrm{Tr}\,(\mathcal{P}_{\vec{x}})^s\right]\\ &= \prod_{\{\vec{x}\}}\mathrm{Det}\,\left(\mathbf{1} - \epsilon\, C\mathcal{P}_{\vec{x}}\right)^2, \quad C = (2\,\zeta)^{N_\tau}, \qquad (2.13) \end{aligned}$$

where $\mathcal{P}_{\vec{x}}$ denotes the Polyakov loop

$$\mathcal{P}_{\vec{x}} \equiv \prod_{t=0}^{N_\tau-1} U_{(\vec{x},t),\mu} \qquad (2.14)$$

and from now on traces and determinants are understood only over the color indices. For later reference we also define the shortening:

$$P \equiv \frac{1}{N_c}\,\mathrm{Tr}\,\mathcal{P}, \quad P^* \equiv \frac{1}{N_c}\,\mathrm{Tr}\,\mathcal{P}^\dagger \qquad (2.15)$$

(notice the different normalization to (2.14) above). In the limit (2.12) μ diverges and the parameter of the model is ζ (2.12) or the related C (2.13) which is directly connected to the average charge density on a non-zero temperature lattice:

$$\hat{n}_0 = \langle\frac{\partial}{\partial\mu}\mathcal{Z}_F^{[0]}\rangle \simeq 2C\langle\sum_{\vec{x}}\mathrm{Tr}\,\mathcal{P}_{\vec{x}}\rangle. \qquad (2.16)$$

One can study the behavior of various quantities, such as gluonic correlation functions and correlation functions involving light quarks on such a static background, much like in the quenched approximation at $\mu = 0$. However, effects expected to be due to the mobility of charges, in particular the possibility of new phases in dependence on the chemical potential cannot be studied here.

Since this limit is obtained in an analytic expansion, we can systematically consider higher order corrections. In the following we shall study the model which is obtained at the next order.

D. Large μ limit in order κ^2 as a model for high density QCD

The fermionic determinant to this order is given by:

$$\begin{aligned} \mathcal{Z}_F^{[2]}(\kappa,\mu,\{U\}) &= \exp\left\{-2\sum_{\{\vec{x}\}}\sum_{s=1}^{\infty}\frac{(\epsilon\, C)^s}{s}\times\right.\\ &\left.\times\,\mathrm{Tr}\left[(\mathcal{P}_{\vec{x}})^s + \kappa^2\sum_{r,q,i,t,t'}(\epsilon\, C)^{s(r-1)}(\mathcal{P}^{r,q}_{\vec{x},i,t,t'})^s\right]\right\}\\ &= \mathcal{Z}_F^{[0]}(C,\{U\})\prod_{\vec{x},r,q,i,t,t'}\mathrm{Det}\,\left(\mathbf{1} - (\epsilon\, C)^r\,\kappa^2\,\mathcal{P}^{r,q}_{\vec{x},i,t,t'}\right)^2. \end{aligned} \qquad (2.17)$$

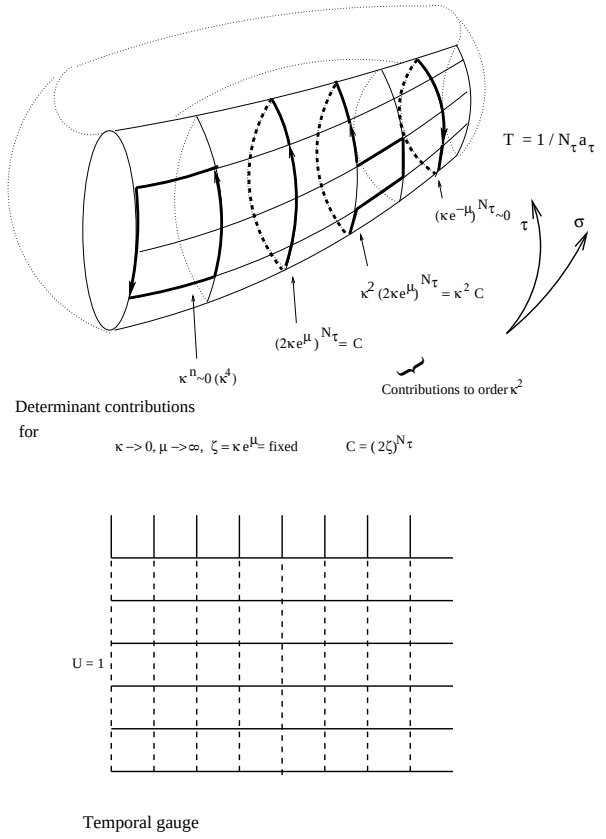


FIG. 1: Periodic lattice, loops, temporal gauge. In the maximal temporal gauge also the links of the basis line are fixed to 1 up to the rightmost one.

The loops contributing to the determinant are shown in Fig. 1. In the following we shall use antiperiodic b.c. ($\epsilon = -1$) to ensure reflection positivity.

For easy bookkeeping we use the temporal gauge

$$U_{n,4} = 1, \text{ except for } U_{(\vec{x},n_4=N_\tau),4} \equiv V_{\vec{x}} : \text{ free}, \quad (2.18)$$

then

$$\begin{aligned} \mathcal{P}^{r,q}_{\vec{x},i,t,t'} &= (V_{\vec{x}})^{r-q} U_{(\vec{x},t),i} (V_{\vec{x}+\hat{\imath}})^q U^*_{(\vec{x},t'),i} \qquad (2.19)\\ & r > q \geq 0,\ i = \pm 1, \pm 2, \pm 3, \\ & 1 \leq t \leq t' \leq N_\tau \ \ (t < t' \text{ for } q = 0)\,. \end{aligned}$$

See [6]. Notice that for $SU(3)$ we have:

$$\begin{aligned} \mathrm{Det}\,(\mathbf{1} + C\,\mathcal{P}) &= 1 + C\,\mathrm{Tr}\,\mathcal{P} + C^2\,\mathrm{Tr}\,\mathcal{P}^* + C^3 \\ &= 1 + 3C\,P + 3C^2\,P^* + C^3\,. \quad (2.20) \end{aligned}$$

Our model is thus defined by using $\mathcal{Z}_F^{[2]}$ for $\mathcal{Z}$ in Eqs.(2.3,2.1) rewritten for general number of flavors n_f. Since $\mathcal{Z}_F^{[2]}$ is factorizable it is easily calculable. It is suggestive to use a splitting Eq. (2.7) preserving the factorization property which would allow to design a local algorithm for producing the C^0 ensemble.

Preliminary results have been reported in [6], [18]. Here we report an extensive analysis of the phase structure of this model at large μ.

III. ANALYTIC COMPUTATIONS

A. Strong coupling/hopping parameter expansion

As a first orientation about the behavior of the model we consider the strong coupling and hopping parameter expansion, which will also serve as a check of the Monte Carlo results. For simplicity we limit ourselves to one flavor here. The expansion proceeds in powers of the parameters β and κ; we are mainly interested in the results for the expectation values $\langle P_{\vec{x}} \rangle$ of the Polyakov loop and its adjoint $\langle P^*_{\vec{x}} \rangle$.

Some details of the computation are given in Appendix A. The results for $\langle P \rangle$ and $\langle P^* \rangle$ to order κ^2 are

$$\begin{aligned} \langle P \rangle^{[2]} \equiv C^2 \frac{1 + \frac{2}{3}C^3}{1 + 4C^3 + C^6} \Bigg[1 + \\ \frac{2\beta\kappa^2(N_\tau - 1)}{3} \frac{2 + 3C^2 + 6C^6}{(1 + 4C^3 + C^6)(3 + 2C^3)} \Bigg] \end{aligned} \quad (3.1)$$

and

$$\begin{aligned} \langle P^* \rangle^{[2]} \equiv C \frac{\frac{2}{3} + C^3}{1 + 4C^3 + C^6} \Bigg[1 + \\ \frac{2\beta\kappa^2(N_\tau - 1)}{3} \frac{(1 + C^3)^4 + 7C^6}{(1 + 4C^3 + C^6)(2 + 3C^3)} \Bigg] . \end{aligned} \quad (3.2)$$

The leading behavior of this for small C is

$$\langle P \rangle^{[2]} \sim C^2 \left(1 + \frac{4}{9}\beta\kappa^2(N_\tau - 1) \right) \quad (3.3)$$

and

$$\langle P^* \rangle^{[2]} \sim \frac{2}{3} C \left(1 + \frac{1}{3}\beta\kappa^2(N_\tau - 1) \right) \rangle\,. \quad (3.4)$$

In Figs. 2 and 3 we compare the results for P and P^* of the Monte Carlo simulations on 4^4 and 6^4 lattices, for $\kappa = 0.12$, one flavor and different values of β, with $P^{[2]}$ and $P^{*[2]}$. The agreement is good for the 4^4 lattice and $\beta = 3$, while for $\beta = 5$ there are already significant deviations. But the agreement between Monte Carlo and strong coupling results is sufficient to validate the simulations. On the other hand, on the 6^4 lattice there is a remarkable difference between $\beta = 5.5$ and 5.6; while in the former case the agreement with the strong coupling expansion remains good up to $\mu \approx 0.95$ at least for $\langle P \rangle$, in the latter case the simulation results start deviating from strong coupling at much lower values of μ. This can be seen as an indication of a phase transition in this region.

B. Mean field calculations

Mean field calculations were quite popular in the early years of lattice gauge theory. They generally gave reasonably good indications of the phase structure of various models, but

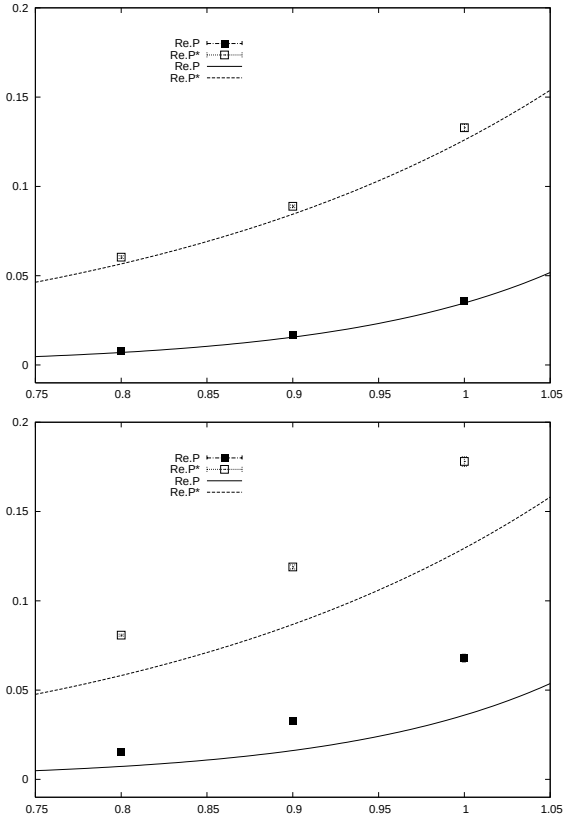


FIG. 2: Comparison with strong coupling at $\beta = 3$ (upper plot) and $\beta = 5$ (lower plot), 4^4 lattice. Full symbols denote ReP, empty symbols ReP^*, the lines show the corresponding strong coupling results.

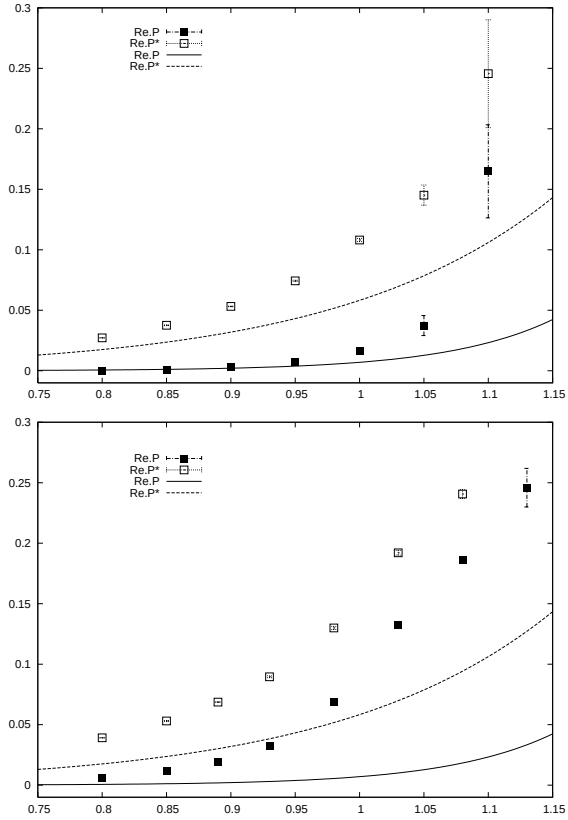


FIG. 3: Comparison with strong coupling, $\beta = 5.5$ (upper plot) and $\beta = 5.6$ (lower plot), 6^4 lattice. Symbols as in Fig.2

with the development of high speed computers and the corresponding improvement of Monte Carlo calculations they fell more or less into oblivion. The reason we are reviving them here is to get some qualitative insight into the phase structure of our model to which the Monte Carlo simulation can be compared. But it should be kept in mind that the method suffers from a certain amount of non-uniqueness and one has to apply it with some common sense. Since the mean field approximation of our model shows some peculiarities and has not been discussed anywhere in the literature, we found it necessary to derive it from the beginning. We summarize here the results and give details in the appendix.

The experience with mean field theory showed that its quality is poor without gauge fixing, but with temporal gauge fixing in pure Yang-Mills theory at zero temperature one gets reasonable results. Since we are dealing here with finite temperature, temporal gauge fixing is not possible. One possibility would be the 'maximal temporal gauge' which requires to fix all temporal links to the identity except in one layer, but applying the mean field approximation would lead to a mean field that is not constant under time translations; this would not only be cumbersome, but probably also a poor approximation since it is violating a basic symmetry of the problem. We take instead the next simplest choice: we fix the temporal gauge field to be constant ('constant temporal' or 'Polyakov gauge'). While the maximal temporal gauge does not lead to a nontrivial Faddeev-Popov determinant, going from that to the constant temporal gauge involves a nontrivial Jacobian (see appendix).

A problem that was noted already in the eighties concerns the temperature dependence of the 'deconfining' phase transition. This is not represented appropriately by the leading mean field approximation if one uses an isotropic lattice and varies T be varying N_τ. We therefore fix (somewhat arbitrarily) β and N_τ and introduce the temperature through anisotropy between spatial and temporal parameters, see Eqs.(2.2),(2.3). There we introduced two anisotropy parameters γ_G and γ_F; in principle they should both be determined as a function of the single parameter γ_{phys} by requiring space-time symmetry at $C = 0$ and $T = 0$. To leading order, however, we may set $\gamma_G = \gamma_F = \gamma_{phys} \equiv \gamma$; this is what was done in the computations in the appendix, since at this stage we cannot determine γ_{phys} and the mean field computations are only meant to give a tentative picture of the phase structure.

The temperature is then related to γ by

$$aT = \frac{\gamma}{N_\tau}\,, \tag{3.5}$$

where the lattice spacing a is in principle determined by β. (Notice that there is now a nonzero minimal temperature.)

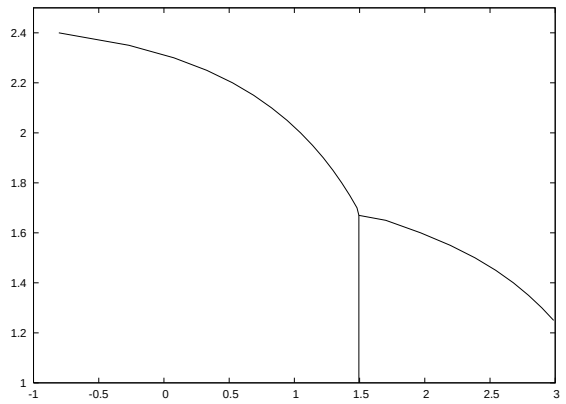


FIG. 4: Mean field phase diagram (abscissa μ, ordinate $\gamma = N_\tau\, a\, T$).

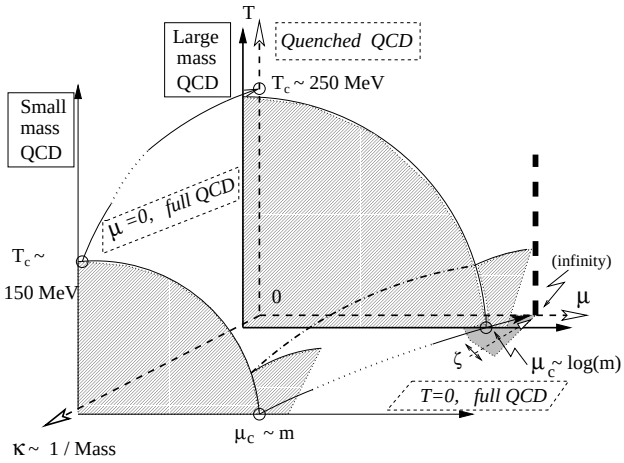


FIG. 5: Tentative phase diagram in T and μ for various κ.

The mean field approximation is expressed in terms of two different mean fields u and v for the spatial and temporal gauge field links, respectively. In Fig.4 we give an illustrative example, taken with $\beta = 4$ and $N_\tau = 6$. It shows a large 'confinement' region for small T and μ corresponding to the trivial fixed point mentioned above with both mean fields u and v vanishing. For larger T or μ one crosses into a deconfined regime with both mean fields $u, v > 0$. In the lower right corner there appears in addition an intermediate phase with $u = 0,\ v > 0$. The field v is close to its maximal value 1 wherever it is nonzero, whereas u has smaller, varying values, depending on the region.

Of course the fact that the mean fields u and v are exactly zero in some regions is an artifact of the mean field approximation; according to earlier experience already the next approximation in the saddle point expansion would eliminate this feature. But qualitatively the mean field results indicate three phases in which different amounts of disorder are present: in the confined phase all the gauge fields are very much disordered, in the intermediate phase the Polyakov loops become ordered, while the spatial gauge fields remain disordered; finally there is the deconfined phase in which all the gauge fields show a high degree of order, but the Polyakov loops represented by v more so than the spatial gauge fields represented by u. In the mean field picture we present here, increasing μ at fixed temperature, one first goes from the confined to the intermediate phase and then from there to the deconfined phase. This may be an artifact of the approximation and in reality the boundary between the intermediate and deconfined phases may go upward. In any case, the simulations to be shown in the next section suggest that by making the chemical potential very large at fixed temperature we end up in the 'half-ordered' phase.

IV. SIMULATIONS AND RESULTS

A. Phase diagram

As stated in the introduction, the model we are studying arises from the double limit $\kappa \to 0$ and $\mu \to 0$ of QCD, keeping $\zeta = \kappa \exp(\mu)$ fixed. It can be seen either as a laboratory to study QCD at large mass density near the quenched limit with a non-zero baryon density or as a model interesting by itself at any value of μ and κ^2, describing a dense system of heavy baryons.

The model still has a the sign problem that is getting more serious with increasing μ. But for not too large values of μ and not too large lattices a local algorithm with a reweighting still converges in reasonable computer time, as will be shown explicitly below. Thus we are able to carry out simulations across large μ "transitions" at T significantly below the deconfining temperature T_c at $\mu = 0$.

The tentative phase diagrams T vs.μ are shown in Fig. 5. Here we show three planes: One corresponds to "quenched" QCD with a finite density of infinitely heavy quarks at $\kappa = 0$. This case has been studied for small N_τ in [4, 5]. At zero density we should find the first order phase transition of pure SU(3) Yang-Mills theory at $T_c \approx 250$ MeV.

The plane in front is the region of κ near the critical value corresponding to masses that are small in lattice units. Here it has been found that there is only a crossover between confined and deconfined phases for all values of $\mu < \mu_c$, $\mu_c \approx 400$ MeV. For $\mu \geq \mu_c$ one expects a sharp transition, curving down towards $T = 0$ with increasing μ [2]. It has been conjectured that at small T above some value of μ a new phase exists, different from the deconfined (quark-gluon plasma) phase; this phase might be describable as a color superconductor and if the number of flavors is $N_c = 3$ "color flavor locking" (CFL) is expected [19].

Our model corresponds to a plane in between, i.e. small but positive κ, to be chosen below; as described in Section II, it is based on an expansion of the hopping parameter up to order κ^2. Since κ is essentially proportional to $1/M$, our model contains some unquenched dymanics due to the fact that we are near but not in the quenched limit $\kappa = 0$. We expect the phase diagram to be similar to the one for small mass just described. To check this is one of the purposes of this study.

We are studying here for $\kappa = 0.12$, mostly the region of high μ, see Fig. 6. In this region the phase diagram in tem-

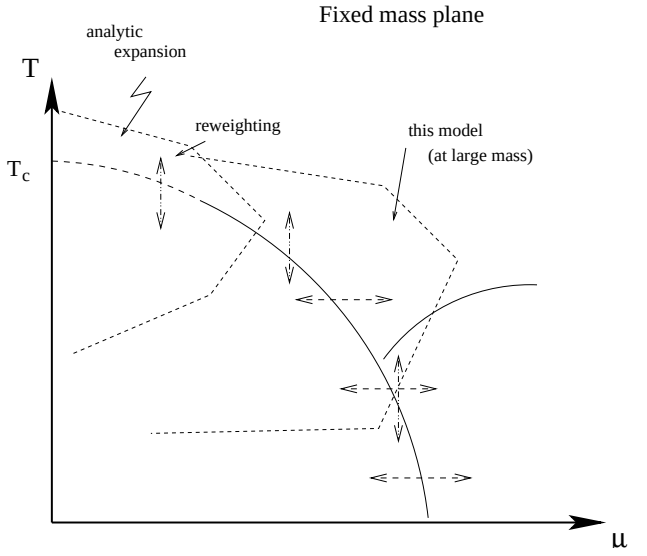


FIG. 6: Fixed mass plane phase diagram; dotted arrows indicate sequences of runs.

perature and chemical potential is expected to have a line of deconfinement transitions running into a triple point at some nonzero μ and T. As mentioned above, at this point two further phase transition lines branch off, separating the new "color superconducting" or color-flavor locked phase from the quark-gluon plasma as well as the confined hadronic phase. It has been a long standing challenge for lattice QCD to explore this region.

B. Observables

We measure several observables under the variation of μ and T, to check the properties of the different phases for small T and large μ. In the following we specialize to $N_c = 3$. The observables are: the Polyakov loop,

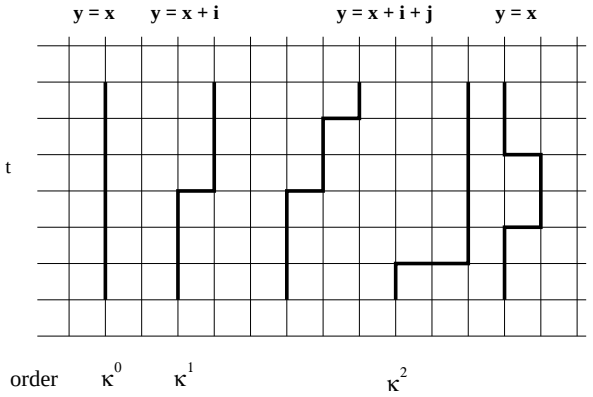
$$\langle P \rangle = \langle \frac{1}{3\,N_\sigma^3} \sum_{\vec{x}} \mathrm{Tr}\, \mathcal{P}_{\vec{x}} \rangle = \langle \frac{1}{N_\sigma^3} \sum_{\vec{x}} P_{\vec{x}} \rangle \,, \qquad (4.1)$$

and its susceptibility

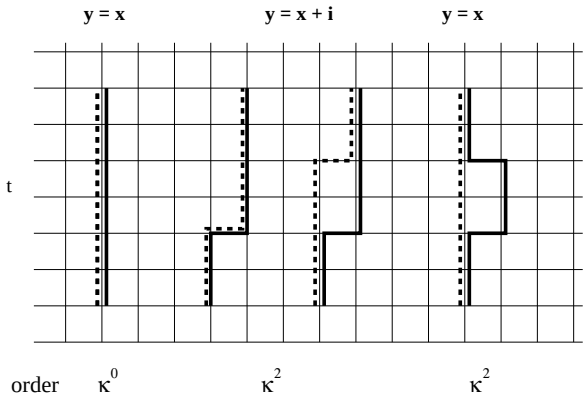
$$\chi_P = \sum_{\vec{y}} \left(\langle P_{\vec{x}}\, P_{\vec{y}} \rangle - \langle P_{\vec{x}} \rangle \langle P_{\vec{y}} \rangle \right) \,, \qquad (4.2)$$

the (dimensionless) baryon number density n_B,

$$n_B = \sum_f \frac{n_{b,f}}{T^3} \,, \qquad (4.3)$$



Contributions to the quark propagator to order $\kappa^2\ \zeta^t$



Contributions to the di-quark propagator to order $\kappa^2\ \zeta^{2t}$

FIG. 7: Paths contributing to quark and diquark "propagators".

where the contribution of each flavor is:

$$\frac{n_b}{T^3} = \frac{N_\tau^3}{3N_\sigma^3}\hat{n} \,, \qquad \hat{n} = \hat{n}_0 + \hat{n}_1 \,,$$
$$\hat{n}_0 = \langle \frac{\partial}{\partial\mu} \mathcal{Z}_F^{[0]} \rangle \approx 2C \langle \sum_{\vec{x}} \mathrm{Tr}\, \mathcal{P}_{\vec{x}} \rangle$$
$$\hat{n}_1 = \langle \frac{\partial}{\partial\mu} \left(\frac{\mathcal{Z}_F^{[2]}}{\mathcal{Z}_F^{[0]}} \right) \rangle \approx 2C\kappa^2 \langle \sum_{\vec{x}} \mathrm{Tr}\, \mathcal{P}_{\vec{x},i,t,t'} \rangle \,, \qquad (4.4)$$

with the corresponding susceptibility

$$\chi_{n_B} = \langle n_B^2 \rangle - \langle n_B \rangle^2 \,, \qquad (4.5)$$

the spatial and temporal plaquettes $\frac{1}{3}\mathrm{Tr}\ P_{\sigma\sigma}$, $\frac{1}{3}\mathrm{Tr}\ P_{\sigma\tau}$ and the topological susceptibility $\chi_{top} = \langle Q_{top}^2 \rangle / (N_\sigma^3 N_\tau)$. The topological charge was measured using an improved field theoretical formula based on five Wilson loops [20]. In order to check the character of the conjectured third phase we also

measure the diquark - diquark correlators

$$C_{(qq)}(\tau) = (\delta_i^a\delta_j^b + \xi\delta_j^a\delta_i^b)(\delta_k^c\delta_l^d + \xi\delta_l^c\delta_k^d)$$
$$\times \sum_{x,y,t} \langle [\psi_i^a \mathcal{C}\psi_j^b(x,t)][\psi_l^c \mathcal{C}\psi_k^d(y,t+\tau)]^\star \rangle$$
$$= (\delta_i^a\delta_j^b + \xi\delta_j^a\delta_i^b)(\delta_k^c\delta_l^d + \xi\delta_l^c\delta_k^d)$$
$$\times \sum_{x,y,t} \Big\{ W^{-1}_{ik;ac}(x,t;y,t+\tau)\mathcal{C}^T W^{-1,T}_{jl;bd}(x,t;y,t+\tau)\mathcal{C}$$
$$- W^{-1}_{il;ad}(x,t;y,t+\tau)\mathcal{C}^T W^{-1,T}_{jk;bc}(x,t;y,t+\tau)\mathcal{C} \Big\}, \quad (4.6)$$

where W^{-1} is the quark propagator measured in maximal temporal gauge, $\mathcal{C}$ the charge conjugation matrix $\{a, \cdots; i, \cdots\}$ the color the flavor indices, respectively, and we have dropped the (summed over) Dirac indices. ξ is a parameter allowing various combinations of color-flavor "locking" (see [19]). Fig. 7 shows the contributions to order $\kappa^2\xi^{2t}$ to quark and di-quark propagators. The corresponding susceptibility is the integral of C_{qq}.

C. Algorithm and simulations

We use the Wilson action and Wilson fermions within a reweighting procedure. The updating is performed with a local Boltzmann factor which only leads to a redefinition of the "rest plaquette":

$$B_0(\{U\}) \equiv \prod_{Plaq} e^{\frac{\beta}{3} Re\mathrm{Tr}\, Plaq} \times$$
$$\times \prod_{\vec{x}} \exp\left\{ 2CRe\mathrm{Tr}\left[\mathcal{P}_{\vec{x}} + \kappa^2 \sum_{i,t,t'} \mathcal{P}^{0,1}_{\vec{x},i,t,t'} \right] \right\}. \quad (4.7)$$

The weight (global, vectorizable) is

$$w(\{U\}) \equiv \prod_{\vec{x}} \exp\left\{ -2\,C\,Re\mathrm{Tr}\left[\mathcal{P}_{\vec{x}} + \kappa^2 \sum_{i,t,t'} P^{0,1}_{\vec{x},i,t,t'} \right] \right\}$$
$$\times\, \mathcal{Z}_F^{[2]}(\{U\}), \quad (4.8)$$

such that,

$$w\, B_0 \;=\; B \;\equiv\; \prod_{Plaq} e^{\frac{\beta}{3} Re\mathrm{Tr}\, Plaq}\, \mathcal{Z}_F^{[2]}(\{U\}).$$

Averages are calculated by reweighting according to Eqs.(2.7), (2.8).

We have employed the Cabibbo-Marinari heat-bath procedure mixed with over-relaxation. This updating already takes into account part of the $\mu > 0$ effects and the generated ensemble can thus have a better overlap with the true one than an updating at $\mu = 0$. One can also use an improved B_0, to be taken care of by a supplementary Metropolis check. Anisotropy can be straightforwardly introduced. Notice that extracting a factor like B_0 may also improve convergence of full QCD simulations at $\mu > 0$.

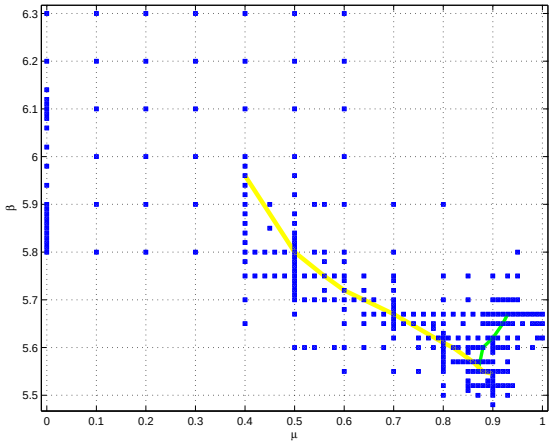


FIG. 8: Data taken in the plane β vs. μ for fixed $\kappa = 0.12$.

The simulations are mainly done on lattice 6^4 for $n_f = 1, 3$ degenerate flavors (any mixture of flavors can be implemented). The κ dependence has been analyzed in [6]. Here we set $\kappa = 0.12$ (rather "small" bare mass $M_0 = 0.167$) which drives the $1/M^2$ effects in the baryonic density to about 50%. The task we have set to ourselves is primarily to explore the phase structure of the model at large chemical potential and "small" temperature and we accordingly vary μ and β. We also want to check the behavior of bulk properties around the prospective "transition" line.

D. Results and discussion

The algorithm works reasonably well over a large range of parameters even at small temperature. The model permits to vary μ, κ, β as independent parameters and it is reasonably cheap to measure various correlations. The region we have analyzed on a 6^4 lattice with $n_f = 3$ is shown in Fig. 8. We have also run simulations on larger and smaller lattices, but we decided to base our discussion on the 6^4 data and also on one value $\kappa = 0.12$. For $8^3 \times 4$ and 8^4 lattices the $n_f = 3$ data are not good enough in the (interesting) high μ region and therefore we do not introduce them in the discussion. All results are expressed in lattice units, and we simulate the temperature variation by varying β according to (2.4) with $\gamma_{phys} = 1$. To avoid the problem of fixing the scale we shall consider T/T_c with T_c of the $\mu = 0$, pure gauge theory. We shall comment on all this in the conclusions.

In Fig. 9 we show the behavior of the baryonic density n_B with β at fixed μ values. We see at the different values of μ inflection points (maximal slope) in β indicating possible qualitative changes of behavior suggesting transitions from low to high temperature phases. In Fig. 10 we vary μ at several fixed β values and see the expected rapid increase of n_B with μ, indicating that we do not see yet saturation effects [21]. Finally, in Fig. 11 we show the "landscape" of the real part of the baryon density (while the imaginary part is compatible with

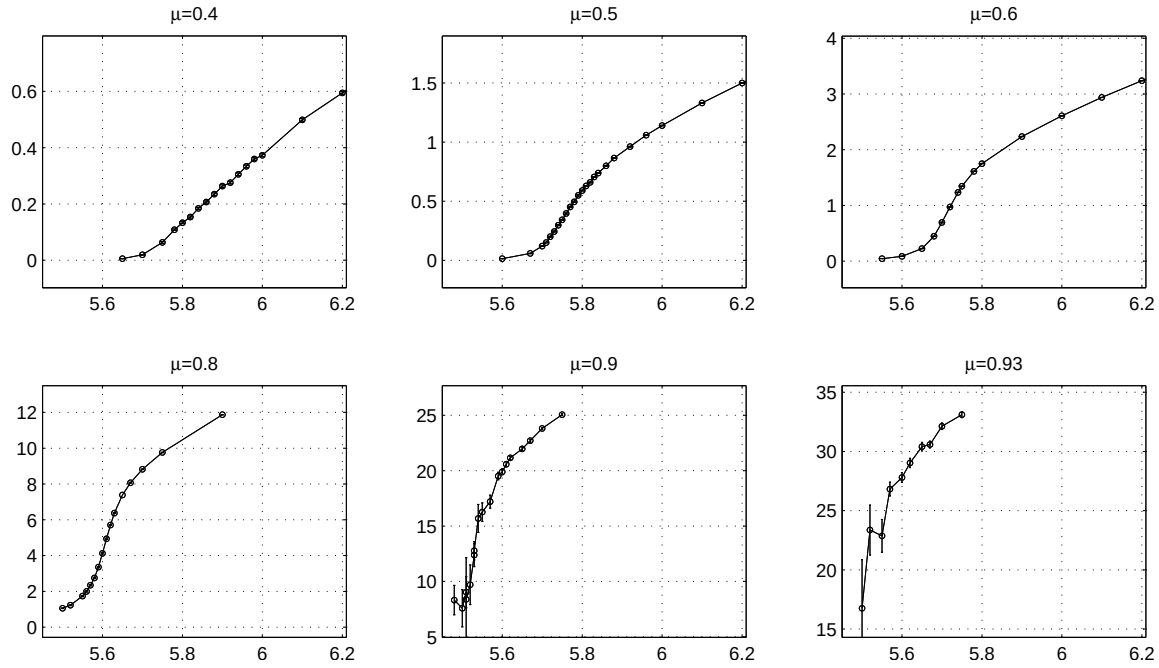


FIG. 9: Baryonic density vs. β at fixed μ.

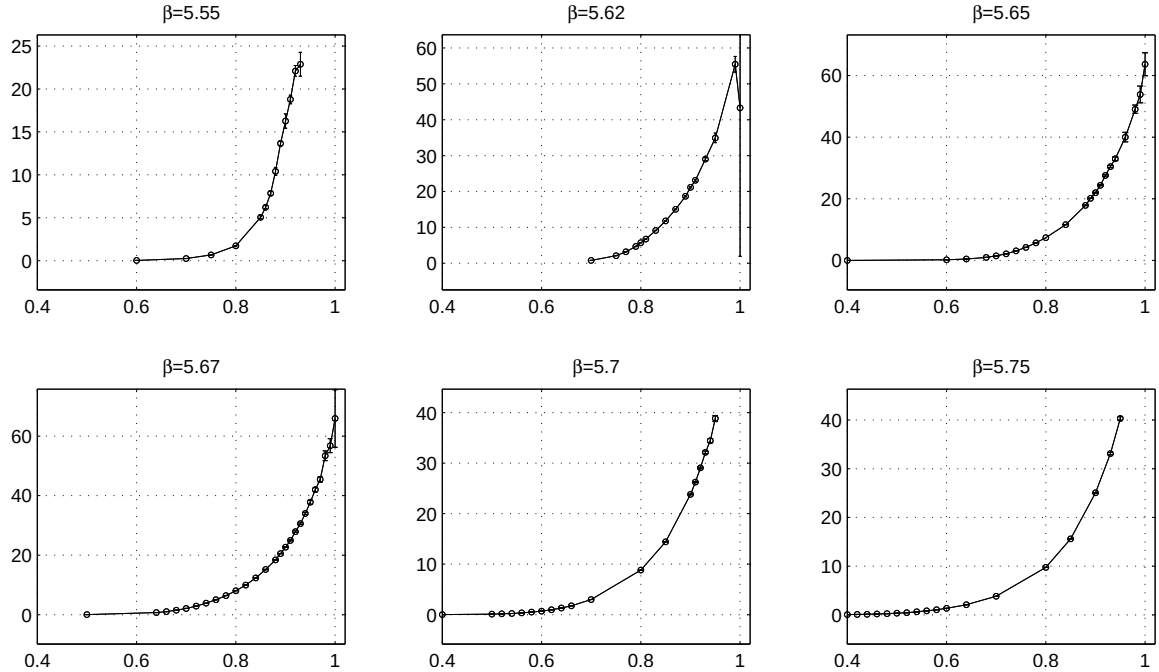


FIG. 10: Baryonic density vs. μ at fixed β.

zero inside the statistical errors, as it should be).

A clearer view of the situation is provided by looking at the "landscape" of the susceptibility of the baryon density, which is shown in Fig. 12. A ridge is clearly visible, highlighted by a dashed black line. A second line (dotted) will be explained later.

The main variation in the baryon density is an exponential growth with μ. This masks to a certain extent the finer structure. We found it therefore advantageous to look at the Polyakov loops and their susceptibility. In Fig. 13 we show this susceptibility at fixed μ vs β and in Fig. 14 at fixed β vs. μ, and in Figs. 15 and 16 the corresponding landscape.

The plots of the Polyakov susceptibility show quite clearly maxima indicating possible transitions or crossovers. In the

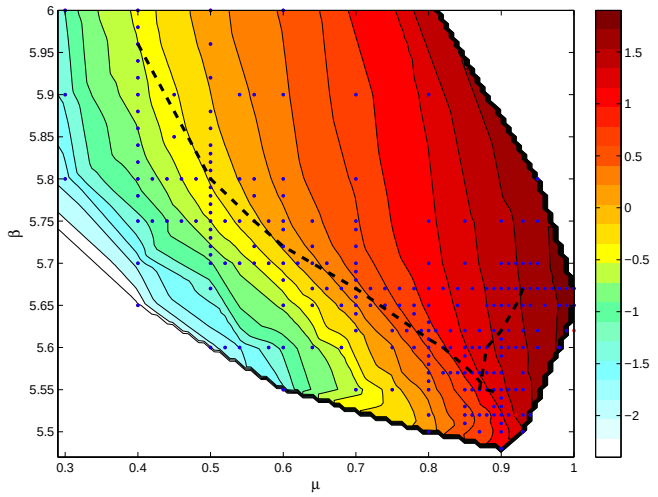


FIG. 11: Landscape of the baryonic density. The color scale (right) is based on $\log_{10}(n_B)$.

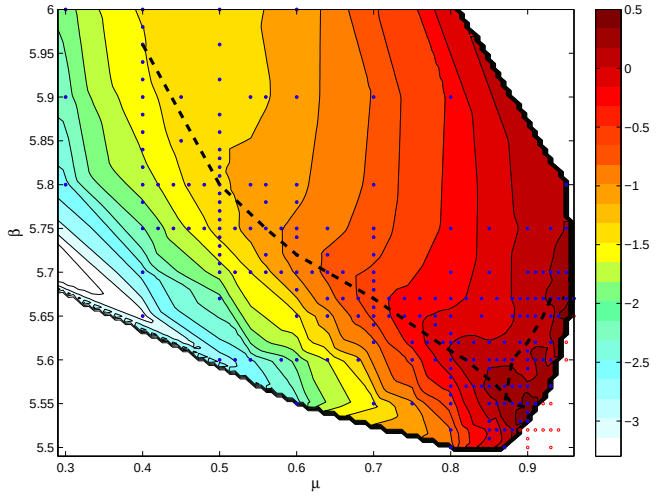


FIG. 12: Landscape of the baryon density susceptibility. The color scale (right) is based on $\log_{10}(\chi_{n_B})$.

landscape Figs. 15 and 16 one of these maxima shows up as a well defined ridge, indicated by a dashed black line. It shows only a moderate slope in μ, which explains why the maxima are more pronounced when we vary β at fixed μ than vice versa. The broadening of this ridge at small μ as well as of the maximum in Fig. 13 is responsible for the loss of a sharp transition signal at small μ. These figures clearly show that the transition at fixed $\mu = 0.50$ is less steep than the one at $\mu = 0.80$. Presumably at $\mu <\sim 0.6$ we are dealing with a crossover, whereas at large μ the signal is more compatible with a real phase transition. Notice that changing β at fixed μ, we cross the transition line at a more oblique angle at smaller μ, but the broadening of the ridge and loss of a transition signal is a genuine effect, as can be seen from Figs. 15 and 16.

A second ridge branching off from this main ridge at large μ, highlighted by a dotted line is suggested by looking at the level lines in Fig. 15 and corresponds to the second maximum suggested at large μ in Fig. 14. This may indicate the appearance of the new phase at large μ and small T/T_c discussed above.

We use the results for the Polyakov loop susceptibility to estimate the possible position of the transition points in the β vs μ plane; to go half way toward a possible physical interpretation the positions determined in this way are indicated by the blobs in the diagram T/T_c vs. μ_{phys}/T_c of Fig. 17, where $\mu_{phys} = \mu/a(\beta) = N_\tau \mu T$ and the relation between β and T/T_c has been roughly estimated from the $\mu = 0$ quenched QCD with $N_\tau = 6$ (we shall comment on this point in the conclusion section). In this figure the axis of the blobs indicate the search lines in the simulation. The shaded blobs correspond to the rather unambiguous 'deconfining' signal observed for $\mu >\sim 0.6$ ($\beta <\sim 5.72$). The 'transition' line suggested by this signal starts at the lower point A on the figure, located at $\beta \simeq 5.55$, $\mu \simeq 0.88$, i.e., with our rough estimation $\mu_{phys}/T_c \simeq 2.4$, $T/T_c \simeq 0.45$ (below which we could no longer obtain reliable data) and ends at the point B located near $\beta \simeq 5.72$, $\mu \simeq 0.6$, i.e., with our rough estimation $\mu_{phys}/T_c \simeq 2.3$, $T/T_c \simeq 0.65$. Above this point the signal becomes ambiguous. But one should keep in mind that moving along lines of fixed μ across a broad ridge, the maximum in general is shifted with respect to the ridge (in our case to lower β values), the location of a transition becomes somewhat blurred, in accordance with the claim that here we are dealing with a crossover and not a phase transition. In Fig. 17 we shaded the upper, 'broad ridge region' above B where the maximum at fixed μ or β deviates significantly from the location of the ridge, which can be easily understood from the landscape Fig. 15. Notice that since we keep κ fixed $\mu = 0$ does not represent the pure Yang Mills theory therefore we did not try to go to this limit. The white blobs correspond to the more volatile, possible 'transition' branching off near point A at large μ, whose signal is strongly affected by fluctuations. We also shaded the region at high μ in the lower right hand corner, where we could not obtain reliable data due to the sign problem.

The picture emerging from the data is thus the following: for $\mu < 0.5 - 0.6$ ($\mu_{phys}/T \sim 3$) there is only a broad crossover, while for $0.6 < \mu < 0.9$ ($3.6 < \mu_{phys}/T < 5.3$) there is evidence of a sharper crossover or transition at a value μ_c depending on β. Moreover, for $\mu \simeq 0.9$ there is some evidence of the presence of the second transition even though this evidence is much weaker than the other one because at larger values of μ the fermion determinant strongly oscillates and, indeed, the usual sign problem manifest its effects.

To get some further insight into the nature of the different regimes or phases we also wanted to look at the distribution of the values of the Polyakov loop in the complex plane. At first we considered the 'histograms' corresponding to the following mathematical expression:

$$H_\Delta(x,y) = \left\langle \Theta_{\Delta,x}\left(\frac{Re(w\,P_{\vec{x}})}{\langle w\rangle_0}\right)\,\Theta_{\Delta,y}\left(\frac{Im(w\,P_{\vec{x}})}{\langle w\rangle_0}\right)\right\rangle_0 \quad (4.9)$$

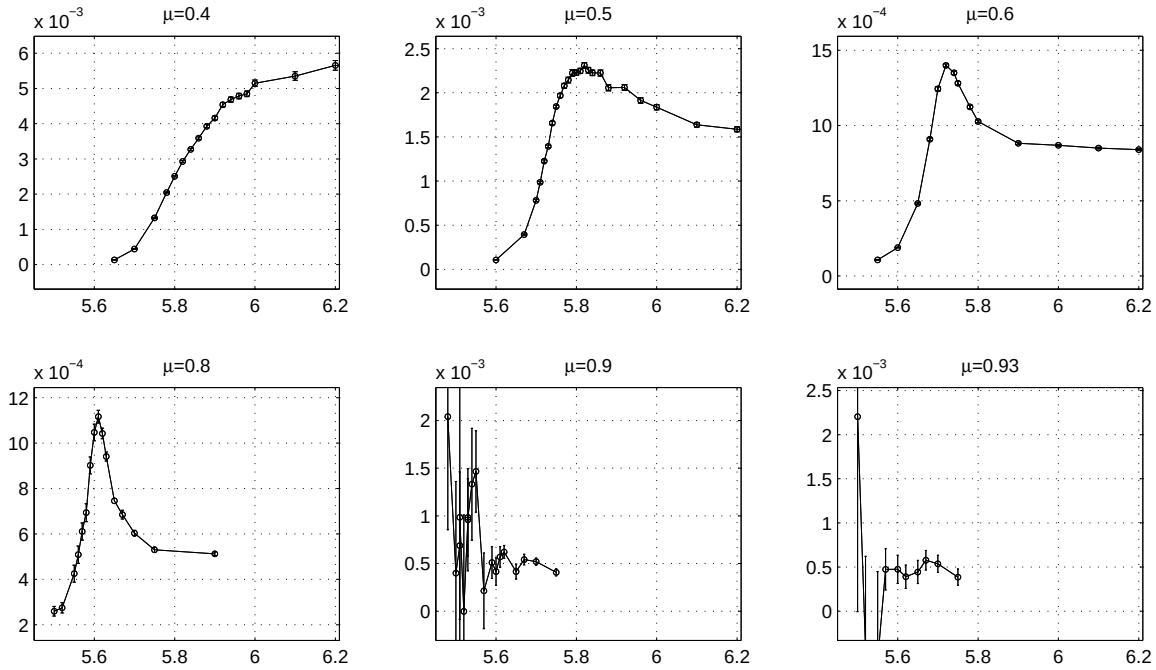


FIG. 13: Polyakov loop susceptibility vs. β at fixed μ.

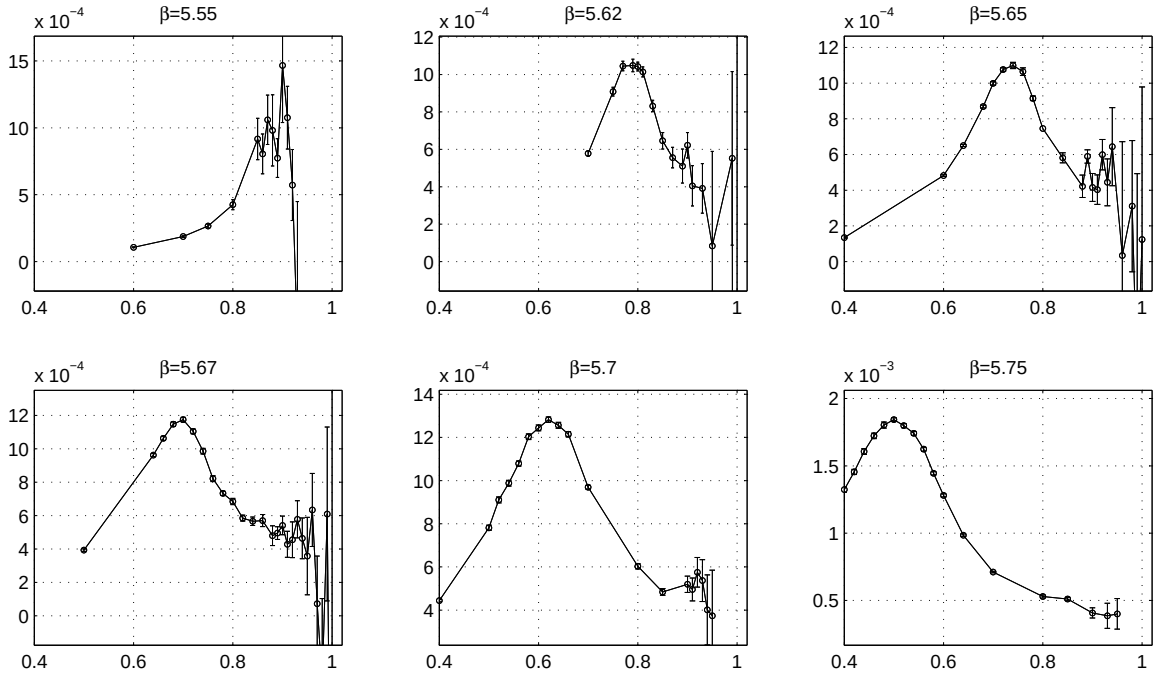


FIG. 14: Polyakov loop susceptibility vs. μ at fixed β.

where $\vec{x}$ is any point in the spatial lattice and $\Theta_{\Delta,s}(t)$ is the function which is 1 if $|t-s| \leq \Delta/2$ and 0 otherwise (the arguments x, y in H should not be confounded with space-time points). For the figures we used 20×20 bins choosing Δ accordingly.These quantities have the advantage that they are positive, because they use the expectation values $\langle . \rangle_0$ determined by the positive Boltzmann factor B_0 (see Eq. 2.7); therefore they can be interpreted as probability distributions. But their disadvantage is that they depend on the choice of B_0. It should also be noted that they describe not really the distribution of the Polyakov loops themselves, but rather the product of the Polyakov loop with the weight factor w; for this reason absolute values larger than 1 are possible and actually occur, as we will see.

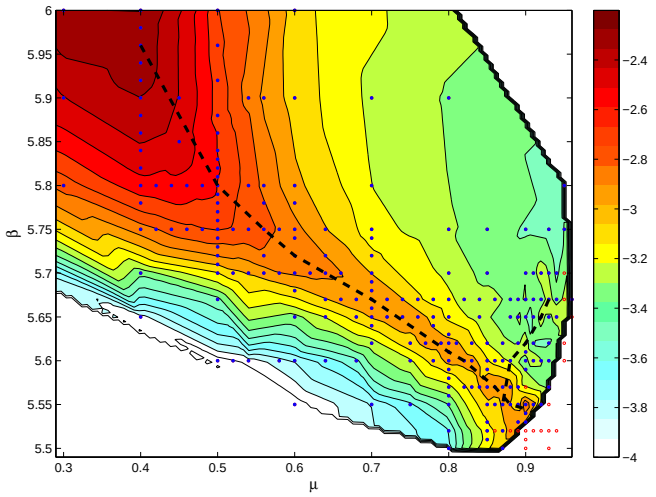


FIG. 15: Landscape of the Polyakov loop susceptibility. The color scale (left) is based on $\log_{10}(\chi_P)$

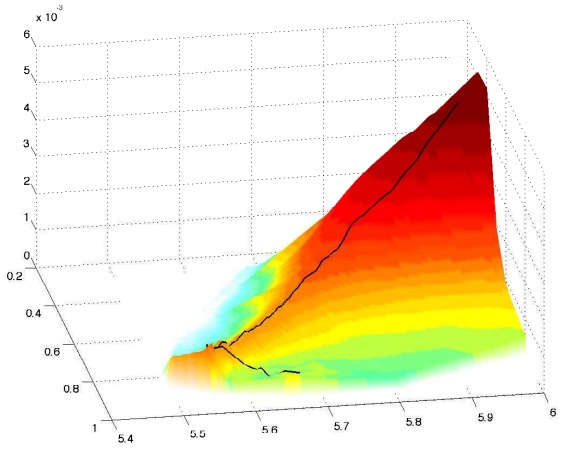


FIG. 16: $3d$ view of Fig. 15.

As an example, see Fig. 18 and Fig. 19 that represent the histogram of H_Δ at different values of μ at $\beta = 5.65$ and different values of β at $\mu = 0.70$, respectively. These figures show different behavior of this observable in accordance with the transition lines indicated in Fig. 17. In fact in Fig. 18 one can discern three different regions: the first one corresponds to $\mu < 0.6$, where the Polyakov loops are concentrated in a small region around zero with only a slight preference for positive real parts; in the second region, for $0.6 < \mu < 0.9$ the Polyakov loops become considerably larger, favoring positive real parts in a significant way, while finally for $\mu > 0.9$ the Polyakov loops (times weight) becomes quite large, but are distributed almost symmetrically around the origin.

This picture can be corroborated by looking at Fig. 19, which according to Fig. 17 should only show one transition. One can see a change of behavior around the point $\beta = 5.65$ (which also occurs in Fig. 18): The Polyakov loops become somewhat larger with a distribution more heavily favoring positive real parts; we interpret this as the transition from a confined to a deconfined phase.

A 'distribution' independent of the choice of B_0 can be defined by considering

$$T_\Delta(x,y) = \langle \Theta_{\Delta,x}(ReP_{\vec{x}})\, \Theta_{\Delta,y}(ImP_{\vec{x}}) \rangle \ , \qquad (4.10)$$

which means adding the weights of all configurations producing a $P_{\vec{x}}$ value in a given bin $|ReP_{\vec{x}} - x| \leq \Delta/2$, $|ReP_{\vec{y}} - y| \leq \Delta/2$. Because now the "expectation value" $\langle . \rangle$ refers to the complex "Boltzmann factor" B (see Eq. 2.7), T_Δ is complex and does not represent a probability distribution. But for small Δ we have

$$\langle P \rangle \approx \sum_{x,y} (x + iy) T_\Delta(x,y) \, , \qquad (4.11)$$

where the sum runs over a lattice with lattice constant Δ in the xy-plane. Since the expectation value of P is real, ReT_Δ has to be even and ImT_Δ odd in y.

We give some representative figures showing the behavior of T_Δ across the putative transitions, for the same parameters as before. Fig. 20 shows ReT_Δ for $\beta = 5.65$ for various increasing values of μ. Again we should observe the crossing of two of the putative transition lines. The transition signals are not very strong, but we can observe that for $\mu < 0.7$ negative real parts are present, which disappear for $\mu \geq 0.7$; at $\mu \geq 0.9$ the real parts become considerably larger again, reaching values of 0.3. Fig. 21 shows ReT at $\mu = 0.7$ for increasing values of β. Here the parameters are such that we should observe only the transition between the hadronic and plasma phases. The indication for this is again that the real parts touch the origin for $\beta \leq 5.65$, whereas for $\beta > 5.65$ they increase to positive values, but staying below 0.2.

Both Fig. 20 and Fig. 21 show that ReT_Δ is to good accuracy even in y, as required for the reality of $\langle P \rangle$. In Figs 22 and 23 we show the imaginary parts of the 'distributions' T_Δ. The qualitative signal of the transitions/crossovers is similar to that of ReT_Δ. It should be noted that now ImT_Δ is, to very good precision, odd in y, again in agreement with the reality of $\langle P \rangle$.

Polyakov loops and charge density (and their susceptibilities), have been the primary quantities used to uncover the phase structure. We also have measured plaquette averages (for both temporal and spatial plaquettes), the topological charge density (using the improved field definition) and quark and di-quark correlators (in maximal axial gauge). All these quantities also some show peculiar behavior in both μ and β which will be exemplified here on two chosen runs, at fixed $\beta = 5.65$ vs. μ and at fixed $\mu = 0.7$ vs. β: In Figs. 24 and 25 we present the dependence of the plaquette averages on μ at $\beta = 5.65$ and on β at $\mu = 0.7$, respectively. We see here clearly the emergence of a physical energy density by the gap developing between the spatial and temporal plaquettes with increasing μ and β; this corroborates the phase picture derived before. In Figs. 26 and 27 we present for the same runs the topological susceptibility whose behavior again is in agreement with the previous conclusions since it decreases in the region where we expect deconfining to set in.

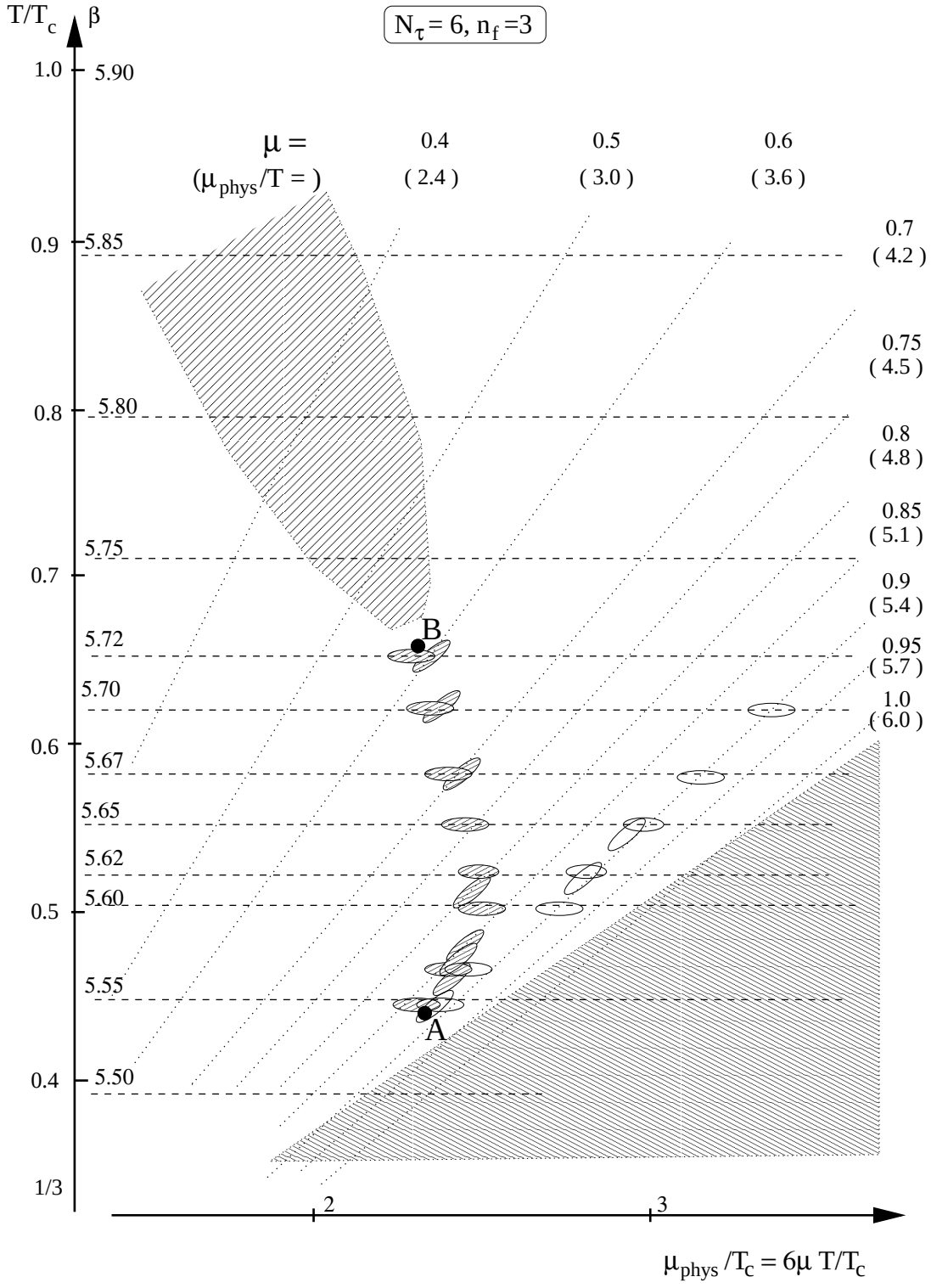


FIG. 17: Phase diagram in the β (or T/T_c) - μ_{phys}/T_c QCD plane. The dotted straight lines correspond to constant μ, the dashed ones to constant β. The blobs, shadowing and other features are explained in the text.

Finally in Figs. 28 and 29 we present the dependence on μ and on β of the diquark susceptibility obtained by integrating the diquark-correlators Eq.(4.6) for $\xi = 0.5$; here we only show the contribution to this susceptibility from the κ^2 terms. This corresponds to quarks showing a (limited) amount of mobility and as can be seen from these figures, the susceptibility to this order is sensitive to the chemical potential (while the zero-th order contribution is dominated by a contact term and

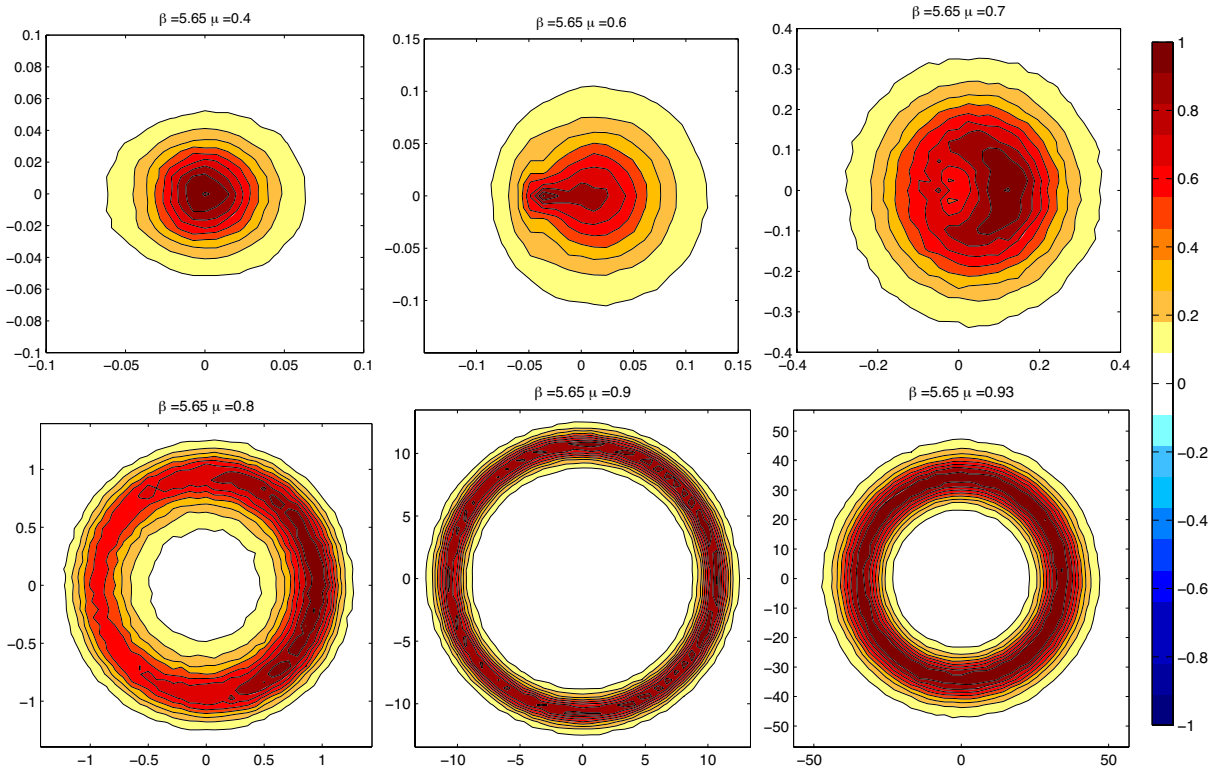


FIG. 18: Polyakov loop 'histogram' $H_\Delta(x,y)$ of eq. (4.9) vs. μ at $\beta = 5.65$.

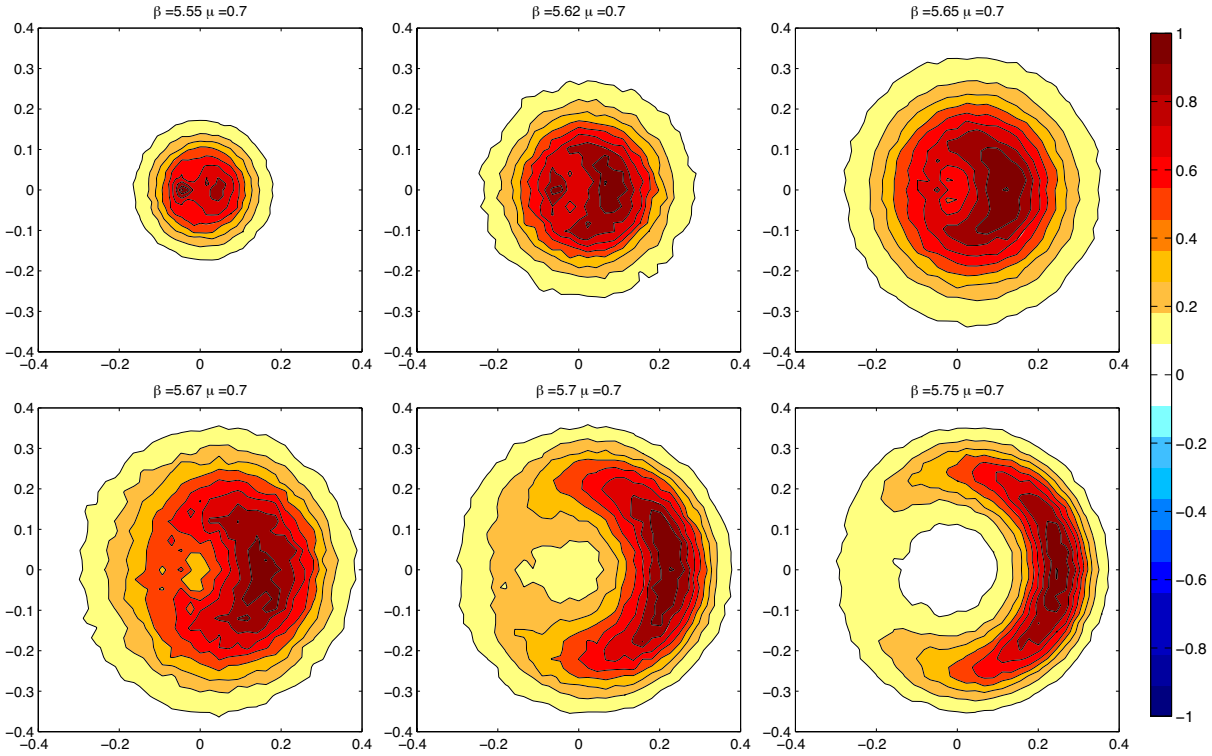


FIG. 19: Polyakov loop 'histogram' $H_\Delta(x,y)$ of eq. (4.9) vs. β at $\mu = 0.70$.

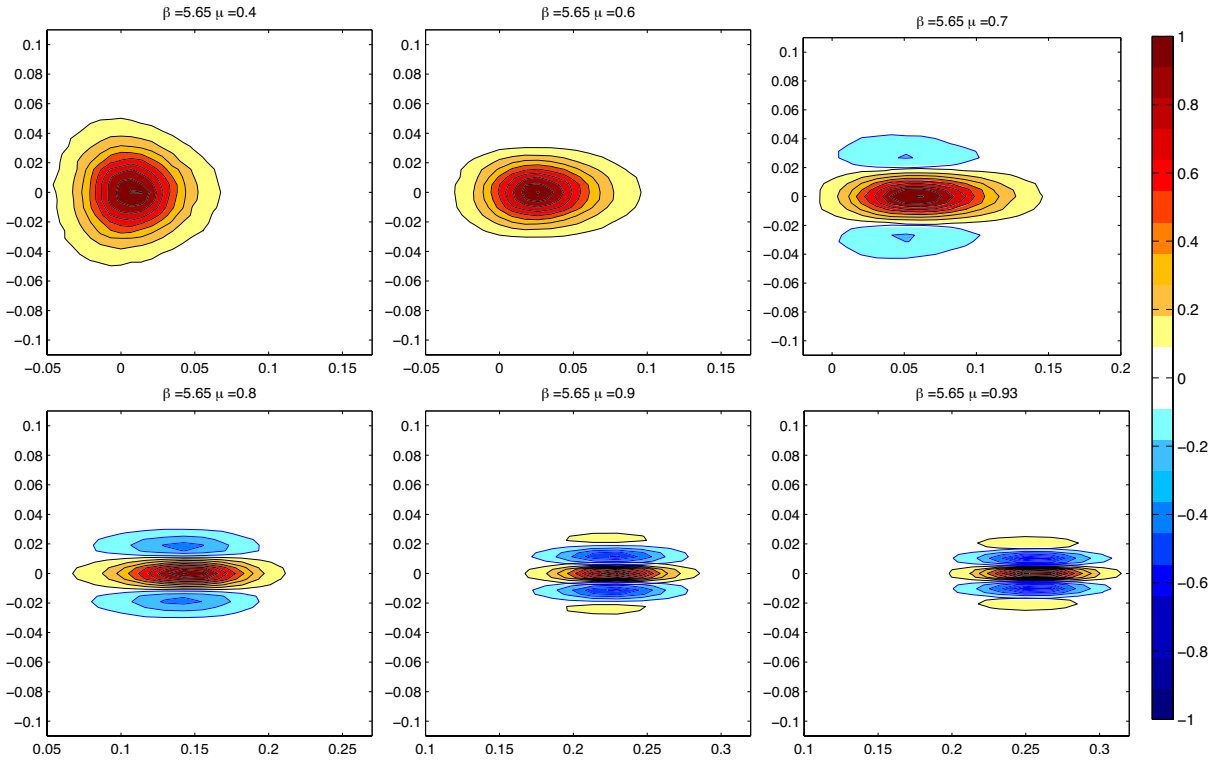


FIG. 20: Real part of the Polyakov loop 'distribution' $T_\Delta(x,y)$ of eq. (4.10) vs. μ at $\beta = 5.65$ fixed.

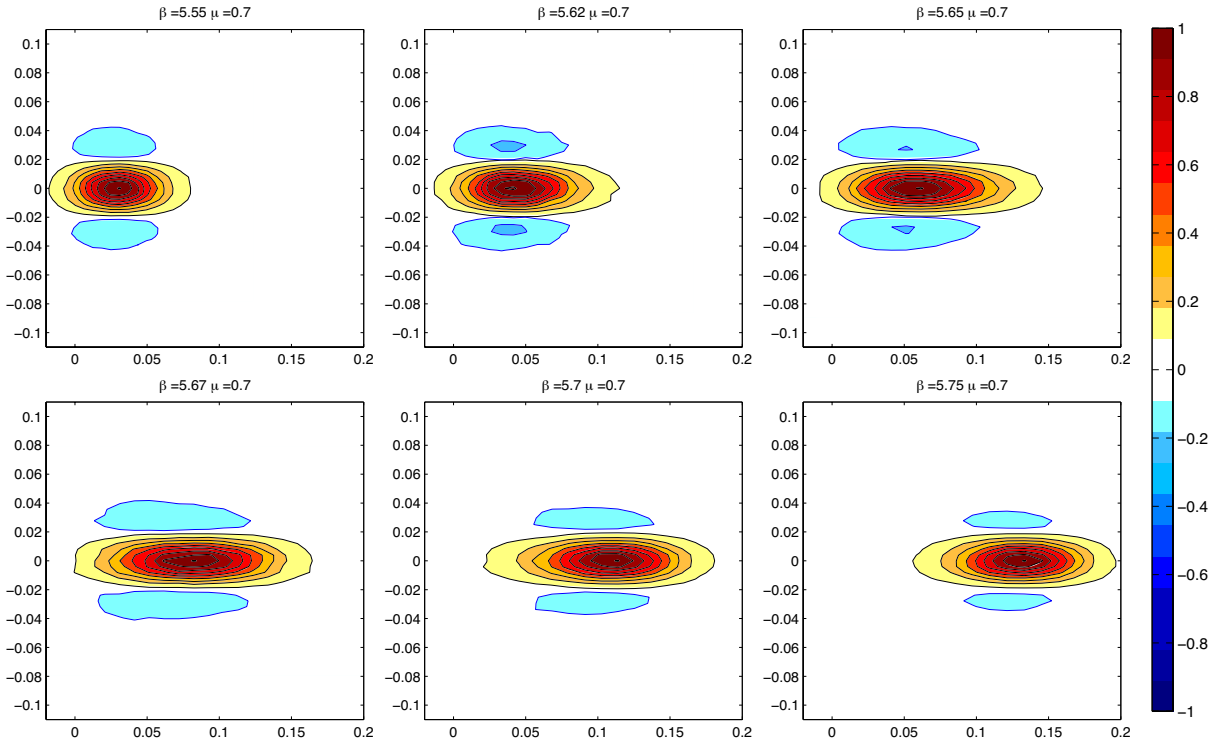


FIG. 21: Real part of the Polyakov loop 'distribution' $T_\Delta(x,y)$ of eq. (4.10) vs. β at $\mu = 0.70$ fixed.

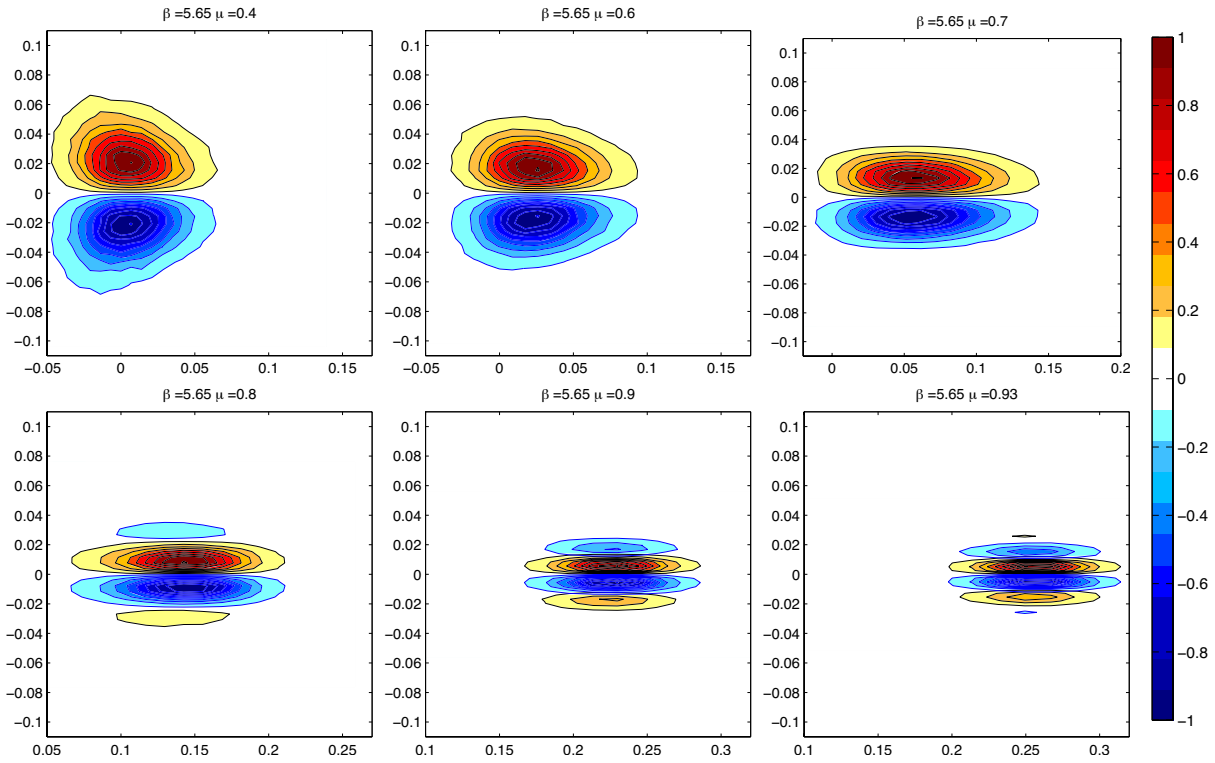


FIG. 22: Imaginary part of the Polyakov loop 'distribution' $T_\Delta(x, y)$ of eq. (4.10) vs. μ at $\beta = 5.65$ fixed.

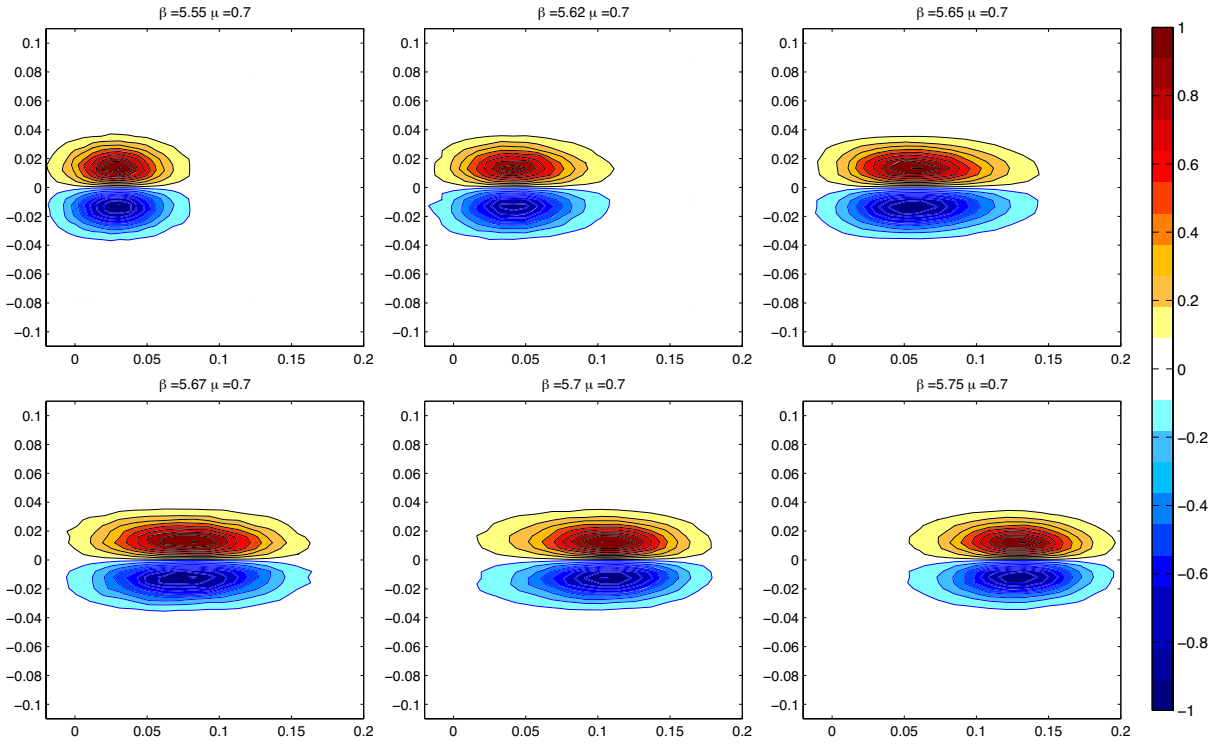


FIG. 23: Imaginary part of the Polyakov loop 'distribution' $T_\Delta(x, y)$ of eq. (4.10) vs. β at $\mu = 0.70$ fixed.

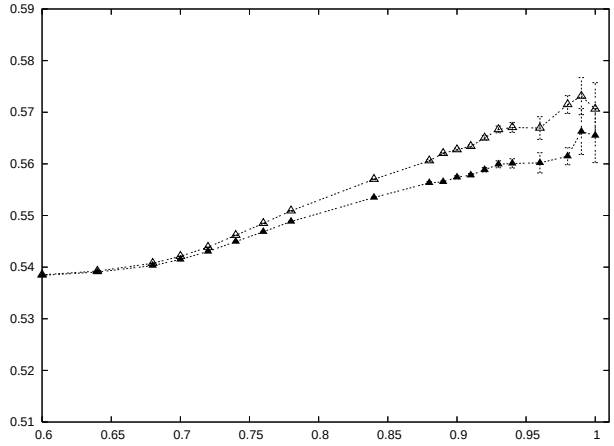


FIG. 24: Plaquette averages vs. μ at fixed $\beta = 5.65$.

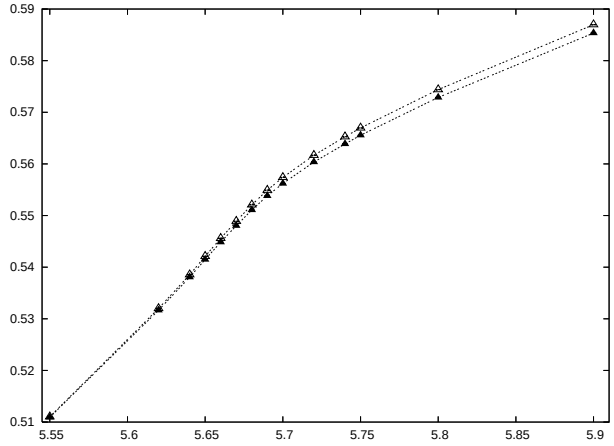


FIG. 25: Plaquette averages vs. β at fixed $\mu = 0.70$.

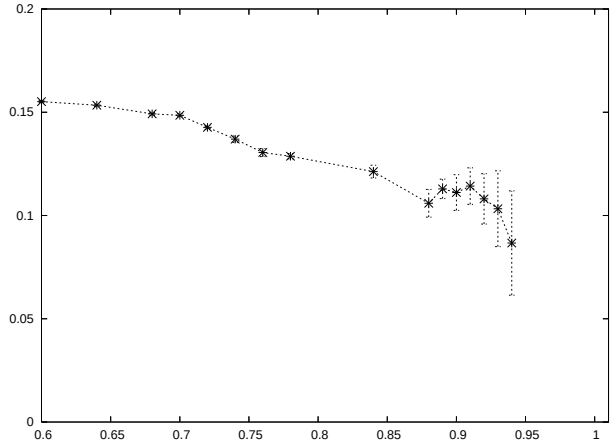


FIG. 26: Topological susceptibility average vs. μ at fixed $\beta = 5.65$.

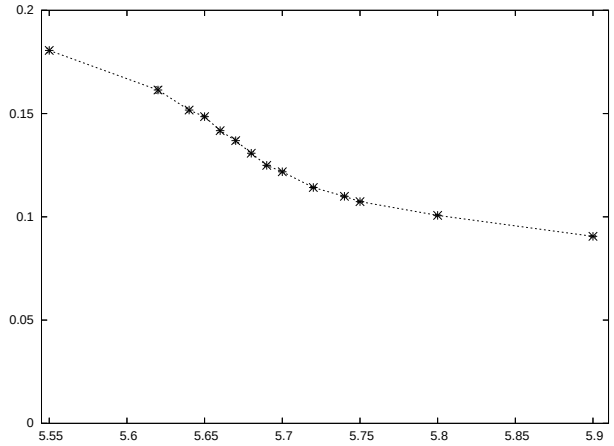


FIG. 27: Topological susceptibility average vs. β at fixed $\mu = 0.70$.

is rather flat). The strong increase with μ, compared with the rather flat β dependence may indicate new properties of the matter at high density.

V. CONCLUSIONS

To obtain analytic informations about our model we first analyzed it via the strong coupling expansion; the agreement for $\beta \leq 5.5$ and small μ with the numerical simulations should be seen as a validation of the simulation program. But our calculations show strong effects at slightly larger μ , which already at $\beta = 5.6$ depart considerably from strong coupling estimates; this is an indication of a possible phase transition. Next we obtained a phase diagram in a mean field approximation, showing the existence of three different phases.

The phase structure found by the numerical simulations for $n_f = 3$ is shown in Fig. 17. The signal for the deconfining transition (or narrow crossover) on the line connecting A and B is rather good and it also appears that at small μ (above B) the transition is smoothed out in accordance with the expectations from full QCD simulations [2],[22]. A second transition at large μ could only be identified tentatively. In this region, the diquark susceptibility grows strongly. This region needs further study to reach a conclusion, but it is interesting that the general picture shows qualitative agreement with the one found in the mean field approximation.

The algorithm works reasonably well over a wide range of parameters and for lattices up to 6^4 (8^4 for $n_f = 1$). We obtain large densities for temperatures $\sim \frac{1}{2} T_c$ or less and reach ratios $\frac{\mu_{phys}}{T} \sim 5$. It appears difficult, however, to go to larger lattices and larger μ with this algorithm and one should consider improving it. For the time being, however, these difficulties precluded us from performing further tests, such as finite size analysis, in order to establish unequivocally the character of the various transitions.

The model permits to vary μ, κ, β and N_τ as independent parameters. Also anisotropic lattices can be envisaged. It is therefore interesting to extend the study to take advantage of this full variability. Also extending the model to higher orders in κ can be envisaged. The bookkeeping soon becomes unmanageable, one could however consider using statistical ensembles of large loops [23].

A related matter is the relation to physical quantities such

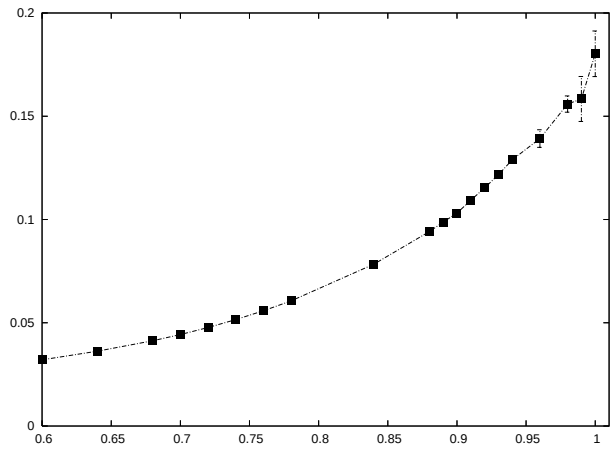


FIG. 28: Diquark susceptibility average vs. μ at fixed $\beta = 5.65$.

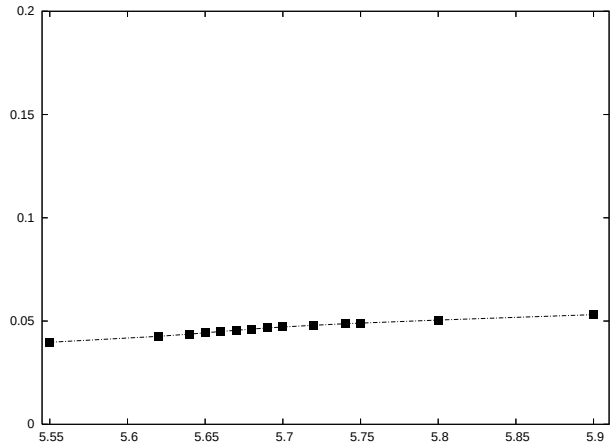


FIG. 29: Diquark susceptibility average vs. β at fixed $\mu = 0.70$.

as temperature and masses. In this study we introduced a T-dependence by varying β and tried to avoid the necessity of defining a scale by considering only dimensionless ratios such as μ_{phys}/T. This, however, has to be taken with a grain of salt: indeed, varying β also introduces varying finite volume and quark 'mass' effects. It would be less ambiguous to vary N_τ if we could reach large enough lattices. Alternatively one could consider using a variable anisotropy. In a first approximation one could take $\gamma_G = \gamma_F = \gamma_{phys}$, such as in the mean field approximation in section III.B, but non-perturbative corrections might be large and a bona-fide calibration may become necessary [9]. All renormalization questions, however, are difficult when we need to consider the effects of the quarks as introduced in fixed order hopping parameter expansion.

Concerning the significance of this analysis we can take two points of view:

Firstly, we can consider this model for itself, as describing 'quasi-static charges' interacting via gauge forces and having a non-trivial phase structure.

Secondly, we can consider this model as an evolved 'quenched approximation' in the presence of charged matter. Then this study would give us information about the modified gluon dynamics of the SU(3) theory in this situation. It would then be natural to think of it as providing a heavy, dense, charged background for propagation of light quarks and calculate light hadron spectra and other hadronic properties under such conditions. This could also help fixing a scale controlling the behavior of the light matter. We consider pursuing work on this subject.

Acknowledgments

We thank P. de Forcrand for helpful criticism of an earlier version of this paper. The calculations have been done on the VPP5000 computer at the University of Karlsruhe and on the PC Cluster at the Physics Department of the University of Parma.

1. Strong coupling expansion: some details

We first calculate the term of order zero, which would vanish trivially without the presence of the chemical potential term C. The fermion determinant to order κ^0 is

$$\mathcal{Z}_F^{[0]} = \prod_{\vec{x}} \det(\mathbf{1} + C\mathcal{P}_{\vec{x}})^2 \,, \tag{A.1}$$

where the determinant only refers to the color degrees of freedom. In order to evaluate this explicitly we introduce the characters χ_σ of the irreducible representations σ of $SU(3)$. In the maximal temporal gauge $\mathcal{P}_{\vec{x}}$ is simply given by $V_{\vec{x}}$ and we find

$$\mathcal{Z}_F^{[0]} = \prod_{\vec{x}} \left(1 + C\chi_3(V_{\vec{x}}) + C^2\chi_{\bar{3}}(V_{\vec{x}}) + C^3\right)^2 \,. \tag{A.2}$$

Using the well-known facts (see for instance [24, 25])

$$\begin{aligned} \chi_{\bar{3}}\chi_3 &= \chi_1 + \chi_8 \,, \\ \chi_3\chi_3 &= \chi_{\bar{3}} + \chi_6 \,, \\ \chi_{\bar{3}}\chi_{\bar{3}} &= \chi_3 + \chi_{\bar{6}} \,, \end{aligned} \tag{A.3}$$

and defining $D \equiv 1 + 4C^3 + C^6$ this becomes

$$\begin{aligned} \mathcal{Z}_F^{[0]} \;=\; & D^{N_\sigma} \prod_{\vec{x}} \Big[1 + \frac{2C + 3C^4}{D}\chi_3(V_{\vec{x}}) \\ & + \; \frac{3C^2 + 2C^5}{D}\chi_{\bar{3}}(V_{\vec{x}}) + \frac{1}{D}C^2\chi_6(V_{\vec{x}}) \\ & + \; \frac{1}{D}C^4\chi_{\bar{6}}(V_{\vec{x}}) + \frac{2}{D}C^3\chi_8(V_{\vec{x}}) \Big] \,. \end{aligned} \tag{A.4}$$

From this it is straightforward to obtain the expectation values $\langle P_{\vec{x}} \rangle$ and $\langle P^*_{\vec{x}} \rangle$ to order 0 as

$$\langle P \rangle^{[0]} = C^2 \frac{1 + \frac{2}{3}C^3}{1 + 4C^3 + C^6} \tag{A.5}$$

and

$$\langle P^* \rangle^{[0]} = C \frac{\frac{2}{3} + C^3}{1 + 4C^3 + C^6} \,. \tag{A.6}$$

The next nontrivial order is $O(\kappa^2)$ in the fermion determinant and comes from the Polyakov loops with one excursion to a neighboring site. A nonzero result is obtained only by combining it with terms from the Yang-Mills action; the lowest nontrivial contribution is therefore $O(\kappa^2\beta)$. Concretely we obtain to order κ^2

$$\frac{\mathcal{Z}_F^{[2]}}{\mathcal{Z}_F^{[0]}} = \left(1 + 2C\kappa^2 \sum_{\vec{x},i,t,t'} \mathrm{Tr}\, \mathcal{P}_{\vec{x},i,t,t'}\right) . \qquad \text{(A.7)}$$

After integrating over the spatial gauge fields U only terms with $t' = t+1$ survive; the integrals occurring are of the form

$$\int dU\, Re\mathrm{Tr}\Big(U_{(\vec{x},t)i} U^\dagger_{(\vec{x},t)i}\Big)\, \mathrm{Tr}\Big(V_{\vec{x}} U^\dagger_{(\vec{x},t)i} U_{(\vec{x},t)i}\Big) = \frac{1}{6}\mathrm{Tr}\, V_{\vec{x}} . \qquad \text{(A.8)}$$

Thus we obtain before the integration over the V's

$$\int \prod dU\, \mathcal{Z}_F^{[2]} = \mathcal{Z}_F^{[0]} \left(1 + \sum_{\vec{x}} \beta\hat{C}\chi_3(V_{\vec{x}})\right) \qquad \text{(A.9)}$$

with $\hat{C} \equiv 2\beta C(N_\tau - 1)\kappa^2/3$. To obtain the expectation values of the Polyakov loops from this we have to expand the product in irreducible characters; we need only the terms involving the representations 3, $\bar{3}$, 1. Using Eq.(A.4) we see that we need a few more decompositions of $SU(3)$ representations, namely

$$\begin{aligned} \chi_3\chi_6 &= \chi_8 + \chi_{10} \\ \chi_3\chi_{\bar{6}} &= \chi_{\bar{3}} + \chi_{\bar{15}} \\ \chi_3\chi_8 &= \chi_3 + \chi_{\bar{6}} + \chi_{15} . \end{aligned} \qquad \text{(A.10)}$$

Since the expectation values are normalized by the partition function, as usual only connected contributions occur; thus the results for $\langle P\rangle$ and $\langle P^*\rangle$ to order κ^2 are

$$\langle P\rangle^{[2]} \equiv C^2 \frac{1 + \frac{2}{3}C^3}{1 + 4C^3 + C^6}\Bigg[1 + \frac{2\beta\kappa^2(N_\tau - 1)}{3}\frac{2 + 3C^2 + 6C^6}{(1 + 4C^3 + C^6)(3 + 2C^3)}\Bigg] \qquad \text{(A.11)}$$

and

$$\langle P^*\rangle^{[2]} \equiv C \frac{\frac{2}{3} + C^3}{1 + 4C^3 + C^6}\Bigg[1 + \frac{2\beta\kappa^2(N_\tau - 1)}{3}\frac{(1 + C^3)^4 + 7C^6}{(1 + 4C^3 + C^6)(2 + 3C^3)}\Bigg] . \qquad \text{(A.12)}$$

We note the leading behavior for small C:

$$P^{[2]} \sim C^2\left(1 + \frac{4}{9}\beta\kappa^2(N_\tau - 1)\right) \qquad \text{(A.13)}$$

and

$$P^{*[2]} \sim \frac{2}{3}C\left(1 + \frac{1}{3}\beta\kappa^2(N_\tau - 1)\right) . \qquad \text{(A.14)}$$

2. Mean Field: some details

We first compute the Faddeev-Popov determinant $J(v)$ for the Polyakov gauge, which can be computed as the Jacobian for the transformation from the maximal temporal to the Polyakov gauge.

The reduced Haar measure for the conjugacy classes $[U]$ of $SU(N)$ is given by [26]

$$d[U] = \frac{1}{\mathcal{N}}\prod_{i<j}\sin^2\left(\frac{\phi_i - \phi_j}{2}\right) d\phi_1 \ldots d\phi_{N-1} , \qquad \text{(A.15)}$$

where $\mathcal{N}$ is a normalization constant; this would be the appropriate measure for the temporal gauge field in the unfixed links of the maximal temporal gauge. We are instead spreading the field uniformly over N_τ links such that we want to integrate over $V \in SU(N)$ with $V^{N_\tau} = U$, so we want to write

$$d[U] = J(V) d[V] , \qquad \text{(A.16)}$$

where $J(V)$ is now the 'quotient' of the Haar measures for V^{N_τ} and U, i.e.

$$J(V) = \prod_{i<j}\frac{\sin^2\left(\frac{N_\tau(\phi_i - \phi_j)}{2}\right)}{\sin^2\left(\frac{\phi_i - \phi_j}{2}\right)} . \qquad \text{(A.17)}$$

So we have to integrate the homogeneous temporal gauge fields with the measure

$$d[V] = \prod_{i<j}\sin^2\left(\frac{N_\tau(\phi_i - \phi_j)}{2}\right)\prod_{k=1}^{N-1} d\phi_k . \qquad \text{(A.18)}$$

The range of integration is the interval $[-\pi, \pi)$ for each ϕ_i; this means of course that V^{N_τ} covers the group $SU(N)$ N_τ times; this 'over-counting' is necessary, since otherwise the integration of functions of V would involve some completely arbitrary choice of the 'N_τth' root.

We now proceed in the standard fashion to produce the mean field theory as a saddle point approximation (see for instance [27, 28]) for the partition function: first the integrals over the group $SU(N)$ are replaced by integrals over the embedding matrix space $M_{N,N}(\mathbb{C})$ by inserting the identities

$$\begin{aligned} 1 &= \int_{M_{N,N}} du\delta(U - u) \\ &= c\int_{M_{N,N}} dM \int_{M_{N,N}} du\, \exp\left[iRe\mathrm{Tr}\, M^\dagger(U - u)\right] \end{aligned} \qquad \text{(A.19)}$$

for each spatial link and similarly for V, introducing the matrix valued fields v and K for each temporal link. The group integrals for the different links are then decoupled and reduce to the one-link integrals

$$\int dU \exp(Re\mathrm{Tr}\, M^\dagger U) \qquad \text{(A.20)}$$

and

$$\int dV\, J(V) \exp(Re\mathrm{Tr}\, K^\dagger V)\ . \tag{A.21}$$

Carrying out the integrals over the gauge field, using these definitions, the partition function reduces to an integral over the matrix valued fields u, v, M, K with an effective action $\tilde{S}(u, v, M, K)$. This integral is suitable for a saddle point approximation. By symmetry there must be a translation invariant extremal of $\tilde{S}$. For the matrix valued fields we furthermore make the ansatz that they are multiples of the identity; by slightly abusive notation

$$\begin{aligned} u &= u\mathbf{1},\ \ v = (v_1 + iv_2)\mathbf{1}, \\ M &= (m_1 + im_2)\mathbf{1},\ \ K = (k_1 + ik_2)\mathbf{1}\ . \end{aligned} \tag{A.22}$$

We anticipated here already that u will be real. Using this ansatz and introducing a single asymmetry parameter $\gamma = \gamma_G = \gamma_F$, as discussed in Section III, the action per site $\tilde{s}$ becomes

$$\begin{aligned} -\ \tilde{s} &= 3\frac{\beta}{\gamma}u^4 + 3\beta\gamma u^2(v_1^2 + v_2^2) \\ &+\ 6C(v_1 + iv_2)^{N_\tau}\left(N_\tau^{-1} + 3(N_\tau - 1)\kappa^2 u^2\right) \\ &+\ 3\ln\zeta(im_1) + \ln\eta(ik_1, ik_2) \\ &-\ 3i(k_1 v_1 + k_2 v_2) - 9im_1 u \end{aligned} \tag{A.23}$$

where the functions ζ and η are defined for arbitrary complex arguments a, b_1, b_2 as

$$\zeta(a) \equiv \int d[U] \exp(aRe\mathrm{Tr}\, U) \tag{A.24}$$

and

$$\eta(b_1, b_2) \equiv \int d[V] J(V) \exp(b_1 Re\mathrm{Tr}\, V + b_2\, Im\mathrm{Tr}\, V) \tag{A.25}$$

For the group $SU(3)$ we write the functions ζ and η in more explicit form:

$$\begin{aligned} \zeta(a) = &\int_{-\pi}^{\pi} d\phi_1 \int_{-\pi}^{\pi} d\phi_2 \rho_1(\phi_1, \phi_2) \\ &\times \exp\left[a(\cos\phi_1 + \cos\phi_2 + \cos(\phi_1 + \phi_2)\right] \end{aligned} \tag{A.26}$$

and

$$\begin{aligned} \eta(b_1, b_2) = &\int_{-\pi}^{\pi} d\phi_1 \int_{-\pi}^{\pi} d\phi_2 \rho_{N_\tau}(\phi_1, \phi_2) \\ &\times \exp\left[b_1(\cos\phi_1 + \cos\phi_2 + \cos(\phi_1 + \phi_2)\right] \\ &\times \exp\left[b_2(\sin\phi_1 + \sin\phi_2 - \sin(\phi_1 + \phi_2)\right]\ , \end{aligned} \tag{A.27}$$

with

$$\begin{aligned} \rho_k(\phi_1, \phi_2) &= \sin^2\left(\frac{k(\phi_1 - \phi_2)}{2}\right)\sin^2\left(\frac{k(\phi_1 + 2\phi_2)}{2}\right) \\ &\times\ \sin^2\left(\frac{k(\phi_2 + 2\phi_1)}{2}\right) \end{aligned} \tag{A.28}$$

When searching for a saddle point we have to allow all parameters to be complex. The saddle point equations, requiring stationarity of $\tilde{s}$ with respect to $u, v_1, v_2, a = im_1, b_1 = ik_1, b_2 = ik_2$ are

$$\begin{aligned} a &= \frac{4}{3}\frac{\beta}{\gamma}u^3 + \frac{2}{3}\beta\gamma u(v_1^2 + v_2^2) \\ &+\ 4C\kappa^2(N_\tau - 1)u(v_1 + iv_2)^{N_\tau}\ , \\ b_1 &= 2\frac{\beta}{\gamma}u^2 v_1 \\ &+\ 2C(v_1 + iv_2)^{N_\tau - 1}(1 + 3N_\tau(N_\tau - 1)\kappa^2 u^2)\ , \\ b_2 &= 2\frac{\beta}{\gamma}u^2 v_2 \\ &+\ 2iC(v_1 + iv_2)^{N_\tau - 1}(1 + 3N_\tau(N_\tau - 1)\kappa^2 u^2)\ , \\ u &= \frac{1}{3}\frac{\mathrm{d}}{\mathrm{d}a}\ln\zeta(a)\ , \\ v_1 &= \frac{1}{3}\frac{\partial}{\partial b_1}\ln\eta(b_1, b_2)\ , \\ v_2 &= \frac{1}{3}\frac{\partial}{\partial b_2}\ln\eta(b_1, b_2)\ . \end{aligned} \tag{A.29}$$

The system of equations is of the form of a fixed point condition and is solved by iteration. There is always a trivial fixed point

$$u = v_1 = v_2 = a = a_1 = b_1 = 0\ . \tag{A.30}$$

In general if there is more than one fixed point (which may be reached by choosing different starting points for the iteration). It turns out that all the fixed points satisfy $a = im_1$ real, $b_1 = ik_1$ purely imaginary, $v_2 = 0$ and u, v_1 real; note that $v_2 = 0$ is consistent with these equations because of the symmetry

$$\eta(b_1, b_2) = \eta(b_1, -b_2)\ , \tag{A.31}$$

which follows from the unimodularity ($d[U] = d[U^\dagger]$).

With our sign convention one always has to choose the fixed point leading to the highest value of the free energy density $f = \tilde{s}$ for the parameters chosen. This leads to discontinuities in the first derivative, typical for first order phase transitions, and finally to the phase diagram shown in Fig.4.

[1] M. G. Alford, hep-lat/0610046.

[2] F. Karsch, J. Phys. Conf. Ser. 46 (2006) 122 [hep-lat/0608003]; Nucl. Phys. A783 (2007) 13 [hep-ph/0610024].

[3] I. Bender, T. Hashimoto, F. Karsch, V. Linke, A. Nakamura, M.

Plewnia, I.-O. Stamatescu, W. Wetzel, Nucl. Phys. Proc. Suppl. 26 (1992) 323.
[4] J. Engels, O. Kaczmarek, F. Karsch, E. Laermann, Nucl. Phys. B558 (1999) 307 [hep-lat/9903030].
[5] T. C. Blum, J. E. Hetrick and D. Toussaint, Phys. Rev. Lett. 76 (1996) 1019 [hep-lat/9509002]; O. Kaczmarek, Ph.D. Thesis, Bielefeld 2000; A. Yamaguchi, Nucl. Phys. Proc. Suppl. 106 (2002) 465.
[6] G. Aarts, O. Kaczmarek, F. Karsch, I.-O. Stamatescu, Nucl. Phys. Proc.Suppl. 106 (2002) 456 [hep-lat/0110145].
[7] R. Hofmann and I.-O. Stamatescu, Nucl. Phys. Proc. Suppl. 129 (2004) 623 [hep-lat/0309179].
[8] P. Hasenfratz and F. Karsch, Phys. Lett. B125 (1983) 308; J. B. Kogut, H. Matsuoka, M. Stone, H. W. Wyld, S. H. Shenker, J. Shigemitsu, D. K. Sinclair, Nucl. Phys. B225 (1983) 93.
[9] G. Burgers, F. Karsch, A. Nakamura, I.O. Stamatescu, Nucl.Phys.B304:587,1988; T. Hashimoto, A. Nakamura , I.O. Stamatescu, Nucl.Phys.B406:325-339,1993.
[10] QCD-TARO Collaboration, Phys. Lett. B609 (2005) 265; Nucl. Phys. A698 (2002) 395.
[11] Ph. de Forcrand, O. Philipsen, Nucl. Phys. B642 (2002) 290 [hep-lat/0205016].
[12] M. D'Elia and M.-P. Lombardo, Phys. Rev. D67 (2003) 014505 [hep-lat/0209146]; M.-P. Lombardo, [hep-lat/0612017].
[13] Z. Fodor and S. D. Katz, Phys. Lett. B354 (2002) 87 [hep-lat/0104001]; JHEP 0404 (2004) 050 [hep-lat/0402006]; S. Ejiri, Phys. Rev. D69 (2004) 094506 [hep-lat/0401012]; Phys. Rev. D73 (2006) 054502 [hep-lat/0506023].
[14] C. R. Allton et al., Phys. Rev. D68 (2003) 014507 [hep-lat/0305007]; S. Ejiri et al, Nucl. Phys. A774 (2006) 837 [hep-ph/0509361]; [hep-lat/0609075].
[15] Z. Fodor, S. D. Katz and C. Schmidt, JHEP 0703 (2007) 121 [hep-lat/0701022].
[16] P. Hasenfratz, F. Karsch and I.-O. Stamatescu, Phys. Lett. B133 (1983) 221; F. Karsch and H. W. Wyld, Phys. Rev. Lett. 55 (1985) 2242; C. Alexandrou et al., Phys. Rev. D60 (1999) 034504 [hep-lat/9811028]; Ph. de Forcrand and U. Laliena, Phys. Rev. D61 (2000) 034502 [hep-lat/9907004]; M. Alford, S. Chandrasekharan, J. Cox and U-J. Weise, Nucl. Phys. B602 (2001) 61-86 [hep-lat/0101012]; R. D. Pisarski, Nucl. Phys. A702 (2002) 151 [hep-ph/0112037]; B.-J. Schaefer, J. M. Pawlowski and J. Wambach, arXiv:0704.3234 (hep-ph).
[17] I.-O. Stamatescu, Phys. Rev. D25 (1982) 1130; I.-O. Stamatescu and T. T. Wu, preprint CERN-TH-6631-92 (1993).
[18] R. De Pietri, A. Feo, I.-O. Stamatescu, E. Seiler, PoS LAT2005 (2006) 170 [hep-lat/0509167].
[19] M. G. Alford, K. Rajagopal and F. Wilczek, Nucl. Phys. B537 (1999) 443 [hep-ph/9804403].
[20] P. de Forcrand, M. Garcia Perez and I.-O. Stamatescu, Nucl.Phys.B499 (1997) 409-449.
[21] S. Hands, S. Kim and J. S. Skullerud, Eur. Phys. J. C. 48, 193 (2006) [hep-lat/0604004 v2].
[22] Y. Aoki, Z. Fodor, S. D. Katz and K. K. Szabo, Phys. Lett. B643 (2006) 46 [hep-lat/0609068].
[23] M. G. Schmidt and I.-O. Stamatescu, Mod. Phys. Lett. A18 (2003) 1499.
[24] C. Itzykson and M. Nauenberg, Rev. Mod. Phys. 38 (1966) 95.
[25] M. Gourdin, Basics of Lie Groups, Éditions Frontières, Gif-sur-Yvette 1982.
[26] H. Weyl, Classical Groups, Princeton University Press, Princeton, N.J. 1946.
[27] J.-M. Drouffe and J.-B. Zuber, Phys. Rept. 102 (1983) 1.
[28] V. F. Müller and W. Rühl, Nucl. Phys. B210 (1982) 289.